UNIVERSITY OF TEXAS ARLINGTON

DOCTORAL THESIS

Exploring Numerical Simulations of Localized Geomagnetic Disturbances

---

Author:
Elizabeth VANDEGRIFF

Supervisor:
Dr. Ramon E. LOPEZ

A thesis submitted in fulfillment of the requirements for the degree of Doctor of Philosophy of Science in the

Department of Physics

May 2023

Declaration of Authorship

I, Elizabeth VANDEGRIFF, declare that this thesis titled, "Exploring Numerical Simulations of Localized Geomagnetic Disturbances" and the work presented in it are my own. I confirm that:

- This work was done wholly or mainly while in candidature for a research degree at this University.
- Where any part of this thesis has previously been submitted for a degree or any other qualification at this University or any other institution, this has been clearly stated.
- Where I have consulted the published work of others, this is always clearly attributed.
- Where I have quoted from the work of others, the source is always given. With the exception of such quotations, this thesis is entirely my own work.
- I have acknowledged all main sources of help.
- Where the thesis is based on work done by myself jointly with others, I have made clear exactly what was done by others and what I have contributed myself.

Signed:

_____

Date:

_____

UNIVERSITY OF TEXAS ARLINGTON

Abstract

Dr. Ramon Lopez and Dr. Dan Welling

Department of Physics

Doctor of Philosophy of Science

Exploring Numerical Simulations of Localized Geomagnetic Disturbances

by Elizabeth VANDEGRIFF

One of the prominent effects of space weather is the formation of rapid geomagnetic field variations on Earth's surface driven by the magnetosphere-ionosphere system. These Geomagnetic Disturbances (GMDs) cause Geomagnetically Induced Currents (GICs) to run through ground-conducting systems. GMDs can often be high amplitude and small-scale (100-500 kilometers) and we classify these as Localized GMDs (LGMDs). LGMDs are both hazardous to the power grid and difficult to predict. Modeling LGMDs is therefore a critical step for risk mitigation but is complicated due to the dynamic and sometimes highly localized nature of the phenomena. At present, global magnetohydrodynamic (MHD) models of the magnetosphere are used in forecasting space weather events, and these models can reproduce LGMDs seen in observation, but the results leave much room for improvement. This study uses a configuration of the Space Weather Modeling Framework (SWMF) model that combines three physical models: Block Adaptive Tree Solar wind Roe Upwind Scheme (BATS-R-US), an ideal MHD model of the magnetosphere; the Ridley Ionosphere Model (RIM), a shell ionosphere calculated by solving 2-D Ohm's Law; and the Rice Convection Model (RCM), a kinetic drift model of the inner magnetosphere. For this study, we use a similar configuration used in Space Weather Prediction Center (SWPC) operations, but with a higher grid resolution which is capable of reproducing mesoscale structure in the tail and ionosphere. In the following work we present a thorough analysis of the ability of the SWMF to reproduce LGMDs in the September 7, 2017 event. Using both metrics defined in previous literature and metrics defined in this study, we quantify the success of the model against

observation over the entire event. We analyze the origins of each LGMD observed in the model and examine the model for features that help us identify drivers of LGMDs. For LGMDs we cannot reproduce, we further explore the model to determine what physical processes are missing from the model that we must add in order to improve our prediction. Finally, we plan for model improvements that will have a direct effect on the ability of the SWMF to reproduce LGMDs.

Acknowledgements

When I started my college journey as a film major, I would never have guessed that almost a decade later I would be completing a doctoral degree in space physics. I was one of the kids who spent a lot of time looking at the night sky; not because it was my idea but because my father would drag us all out of bed at 3 A.M every so often to look at a meteor shower. Jokes aside, my family's dedication to the sciences set me up for an exciting graduate school experience and science career. I am thrilled that I retained the sense of wonder that the vastness and emptiness of space encouraged in me, and along the way I discovered just how much more vast and way less empty space is than I had always imagined as a child.

I want to acknowledge the mentorship and support I received from my professors - most importantly my advisors Professor Dan Welling and Professor Ramon Lopez but also the professors in the UTA Physics Department who taught and guided me through classes and research.

I also want to thank the vibrant Geospace Environment Modeling community for making me feel like I belonged even before I started graduate school. I have learned so much, traveled all over, and met fantastic people. I specifically want to thank Mei-Yun Lin, Agnit Mukhopadhyay, and Sophie Graf. Mei-Yun served with me as GEM Student Representative and has been a big inspiration for the way I engage in leadership. Agnit has supported me every step of the way no matter where in the world he happened to be. I would not have made it this far without his unwavering friendship and motivation. Sophie has been

my friend and conference buddy all through grad school, whether in Texas or at Michigan, and she has played a crucial role in encouraging and supporting me.

Most importantly, I want to thank my lovely wife Christina for sticking by my side through the best and worst parts of graduate school. She is my most constant supporter, and her confidence in me has gotten me through tough times over and over again. She has sacrificed and offered so much, including moving across the country multiple times with me as I pursue my path in the sciences and proofreading last-minute manuscripts that I send her. I will be forever grateful.

Contents

List of Figures

List of Tables

Dedicated to my wife Christina, who is my biggest supporter but most importantly my editor and proofreader.

Chapter 1

Introduction

1.1 Space Weather

Most people are aware of the basic effects that the Sun has on Earth. As well as providing the entire spectrum of visible light, the Sun is the main driving force of Earth's weather patterns, ecosystem, and beach day sunburns. However, there are additional effects that the Sun has on Earth and its environment, ranging from mild to life-threatening, that many remain unaware of. This dissertation focuses on the set of Sun-Earth interactions known as space weather, and as we continue to advance technology and learn more about our solar system it becomes more apparent that understanding and predicting space weather is crucial to protecting ourselves and our technology.

Space weather begins at the solar surface, where high-speed plasma erupts from the Sun due to coronal mass ejections, solar flares, and high-speed streams. This plasma moves through the solar system in tandem with the Sun's magnetic field, which as it moves away from the sun becomes the Interplanetary Magnetic Field (IMF) (Baumjohann & Treumann, 2012). This combination of plasma and

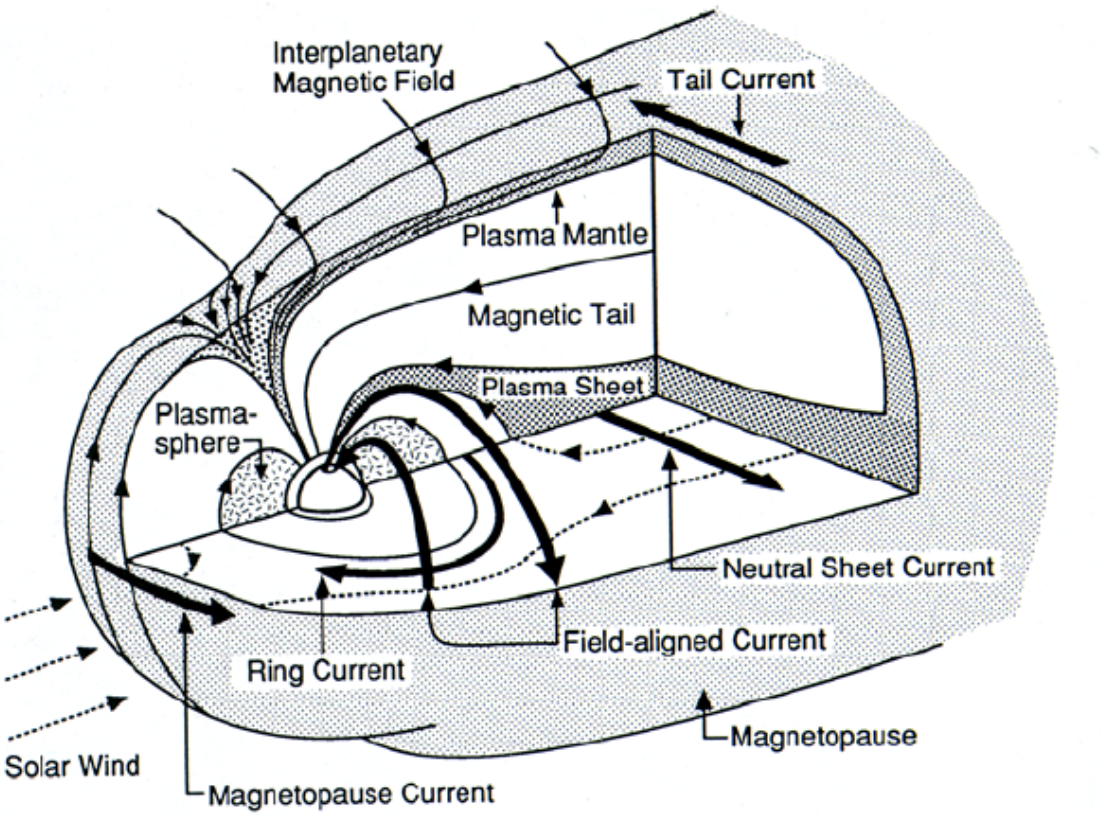

FIGURE 1.1: Anatomy of Earth's magnetosphere. Solar wind compresses the dayside and stretches the nightside to form the familiar shape of the magnetosphere. Within the magnetopause, plasmas with varying energies convect to form different regions with different currents. (Kivelson et al., 1996)

IMF constitutes the solar wind.

1.1.1 Effects on the Magnetosphere

When the solar wind reaches Earth, it interacts with and distorts Earth's magnetic field. Figure 1.1 shows the anatomy of the magnetosphere, beginning with the sunward-facing side of Earth. Here the solar wind makes contact with the magnetosphere at the magnetopause, compressing the dayside of the dipole

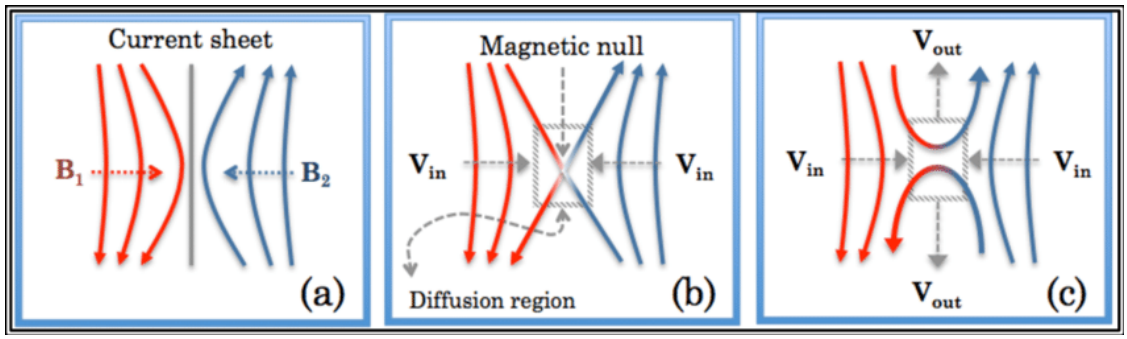

FIGURE 1.2: Magnetic reconnection geometry that happens on both the nightside and dayside of Earth. Frame (a) shows two magnetic field lines moving toward the current sheet between them. Frame (b) shows the two field lines reconnecting. Frame (c) shows the newly reconnected field lines convecting away and carrying plasma with them. (Genestreti et al., 2012)

field. On the other side of Earth, facing away from the sun, the dipole field is stretched into a magnetotail (Dungey, 1961; Gombosi & Holman, 1999; Kivelson et al., 1996).

As the IMF interacts with Earth's magnetic field, a process called magnetic reconnection takes place both on the dayside and the nightside. Figure 1.2 shows reconnection happening as opposing magnetic field lines meet and break away as a single field line, transporting and convecting plasma in the process.

Within the magnetosphere, a multitude of dynamic plasmas and currents interact and form different regions. The ring current, seen in Figure 1.1, is formed by high-energy particles moving along gradient-curvature drifts and forming a westward current in the equatorial plane (Baumjohann & Treumann, 2012). During periods of solar activity, the formation of the ring current causes a magnetic disturbance on the ground that we measure and use to estimate the strength of storms. We call this the Disturbance storm time (Dst) index and calculate it by

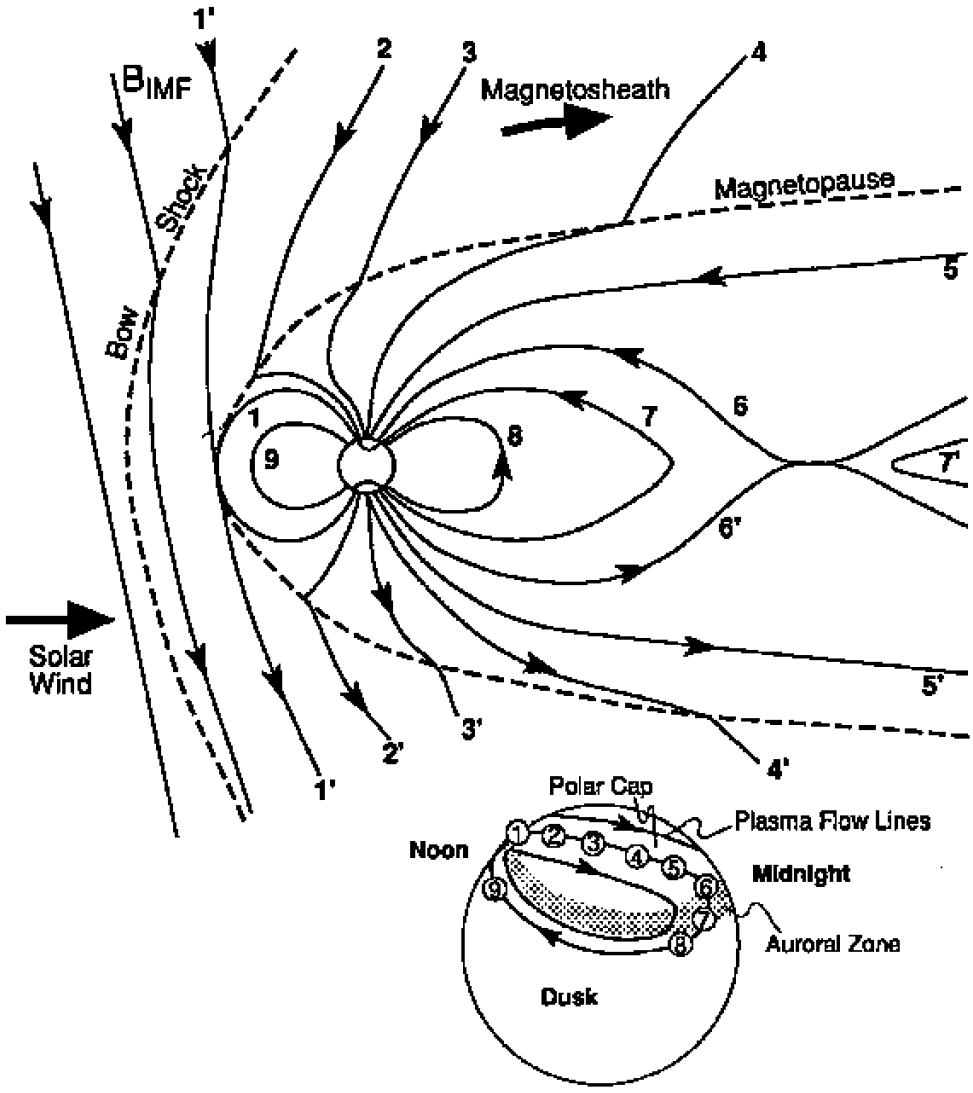

FIGURE 1.3: Progression of the Dungey cycle steps 1-9, starting with dayside reconnection. Ionospheric convection mirrors the cycle of the magnetospheric field lines. (Kivelson et al., 1996)

averaging the global horizontal field variation from four low-latitude magnetometer stations (Russell et al., 1974). Another index that measures the strength of the ring current is the SYMmetric disturbances for H-component (Sym- H) index, which is calculated similarly but with more magnetometers and shows dynamic pressure variations more clearly than Dst (Wanliss & Showalter, 2006).

With a southward-oriented IMF, reconnection drives plasma convection throughout the magnetosphere. Figure 1.3 shows the different stages of the Dungey cycle (Dungey, 1963) from stages 1-9, which describes the progression of this convection. At the bow shock, magnetic field lines "break" and connect with the solar wind, becoming "open" field lines and causing the location of the magnetopause to move Earthward. Open field lines sweep behind Earth and reconnect in the tail. This process converts the energy stored in magnetic field lines into kinetic energy and heating of plasma, which causes plasma to precipitate into the ionosphere.

When the reconnection rate is greater on the dayside than the nightside, the amount of open flux in polar cap grows. For southward IMF, this produces a convection pattern that is tied to a return flow from the distant tail reconnection region to the inner magnetosphere. This kind of convection is inherently unstable (Erickson & Wolf, 1980), and it generally leads to the creation of a near-Earth reconnection region to release the magnetotail stress. The release of this energy powers a phenomenon called a substorm (Baker et al., 1996), which is a fundamental response of the magnetosphere to southward IMF in the solar wind. If the IMF remains southward for an extended period, a magnetic storm results (Gonzalez et al., 1994).

Substorms are characterized by the formation of bright auroral features that spread eastward and (particularly) westward, injections of energetic (100s of KeV) particles into the inner magnetosphere, bursty bulk flows in the magnetotail, the formation of one or more substorm current wedges, and corresponding increases in the westward electrojet (Baker et al., 1996). In particular, substorms are a known driver of electrojet enhancements, which are particularly relevant to this dissertation because they can be the source of intense, localized magnetic perturbations.

In the ionosphere, the effects of the Dungey cycle manifest as an induced electric field with a two-cell convection pattern. This convection pattern depends on the hemisphere and the orientation of the IMF. Birkeland Currents (or Field-Aligned Currents (FAC)) that run along mangetic field lines and close through the ionosphere provide a coupling between magnetosphere and ionosphere. Fig 1.4 shows the Region I currents, which are driven by the solar wind, and the Region II currents, which are driven by pressure balance in the magnetosphere (Cowley, 2000). Region I and Region II currents are two important drivers of auroral and ground processes (Lysak, 1990).

Figure 1.4 shows both horizontal currents. Hall currents are caused by ion drift motion and follow a two-cell convection pattern. Pedersen currents are caused by electron drift motion and close the FAC over the polar cap. The strength of Hall and Pedersen currents are determined by Hall and Pedersen conductance, respectively, in the ionosphere (Ridley et al., 2004). Conductance describes the amount of resistance to plasma moving through the ionosphere.

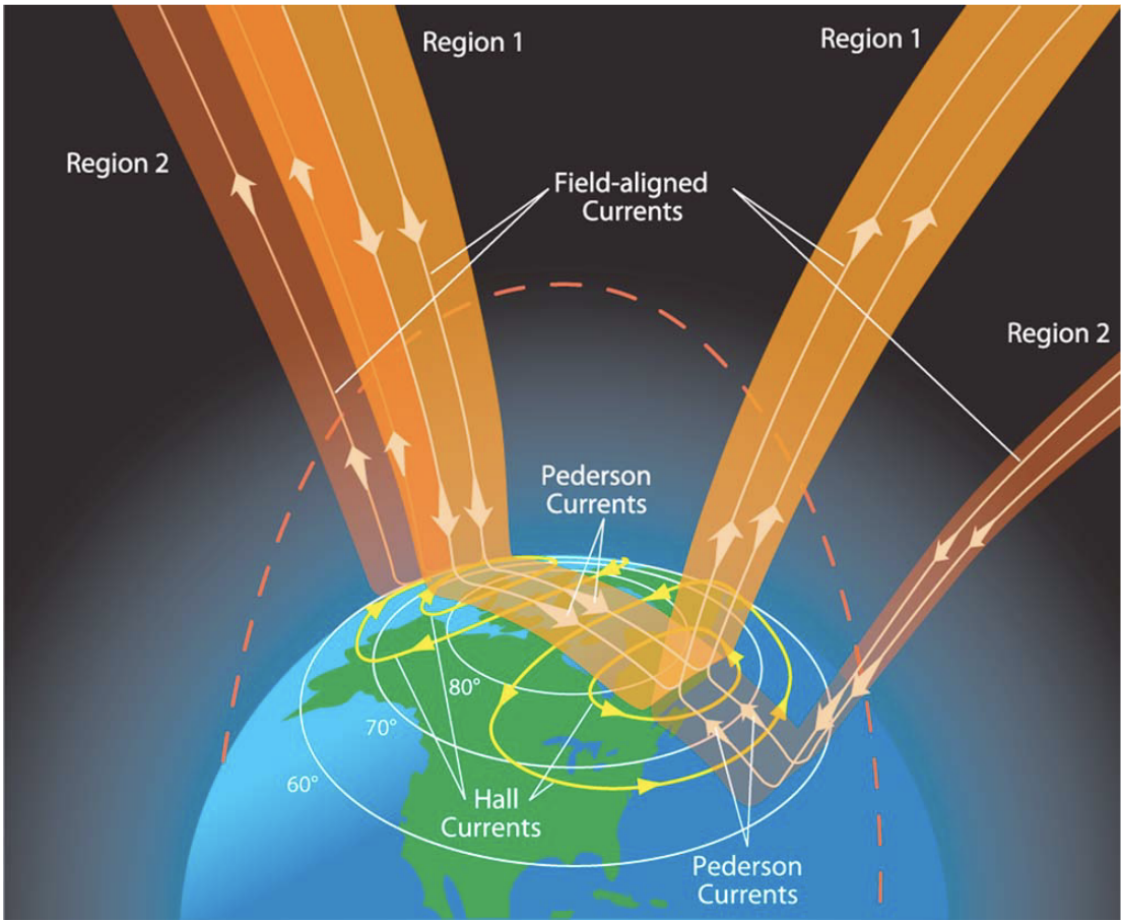

FIGURE 1.4: Ionospheric current system. Field-Aligned Currents close through the ionosphere, and Hall and Pedersen currents flow horizontally. (Le et al., 2010)

Conductance is dependent on a number of sources, including solar Extreme Ultraviolet Radiation (EUV) which affects the amount of ions and electrons present in the ionosphere. Extreme ultraviolet radiation ionizes particles in the upper atmosphere and increases conductivity, which in turn allows stronger currents to flow through the magnetosphere and close in the ionosphere. Particle precipitation into the upper atmosphere, more commonly known as aurora, also affects conductance due to the ionization of particles. Currents connected to conductance are highly dynamic and drive a multitude of effects on the ground.

1.1.2 Effects on the Ground

Magnetospheric and ionospheric response to solar events is highly complex and creates a number of hazards to humans and equipment in this environment. However, these disturbances in geospace can propagate down to Earth's surface, where they can cause harm in a multitude of systems. Figure 1.5 shows the tangible effects of Space Weather on and around Earth. Most relevant in this dissertation are the Geomagnetically Induced Currents (GICs) that run through the ground. GICs are caused by induced geoelectric field variations which are in turn caused by Geomagnetic Disturbances (GMDs) on the ground (Ngwira & Pulkkinen, 2019). Combined with conductivity on Earth's surface, these magnetic fluctuations send GICs can run through man-made ground conducting systems such as railways and power lines, damaging infrastructure and triggering a range of intensely adverse effects (Boteler et al., 1998; Kappenman, 1996; Molinski, 2002). For example, GICs can damage power grid transformers, which can lead to widespread power outages (Ngwira & Pulkkinen, 2019). One such

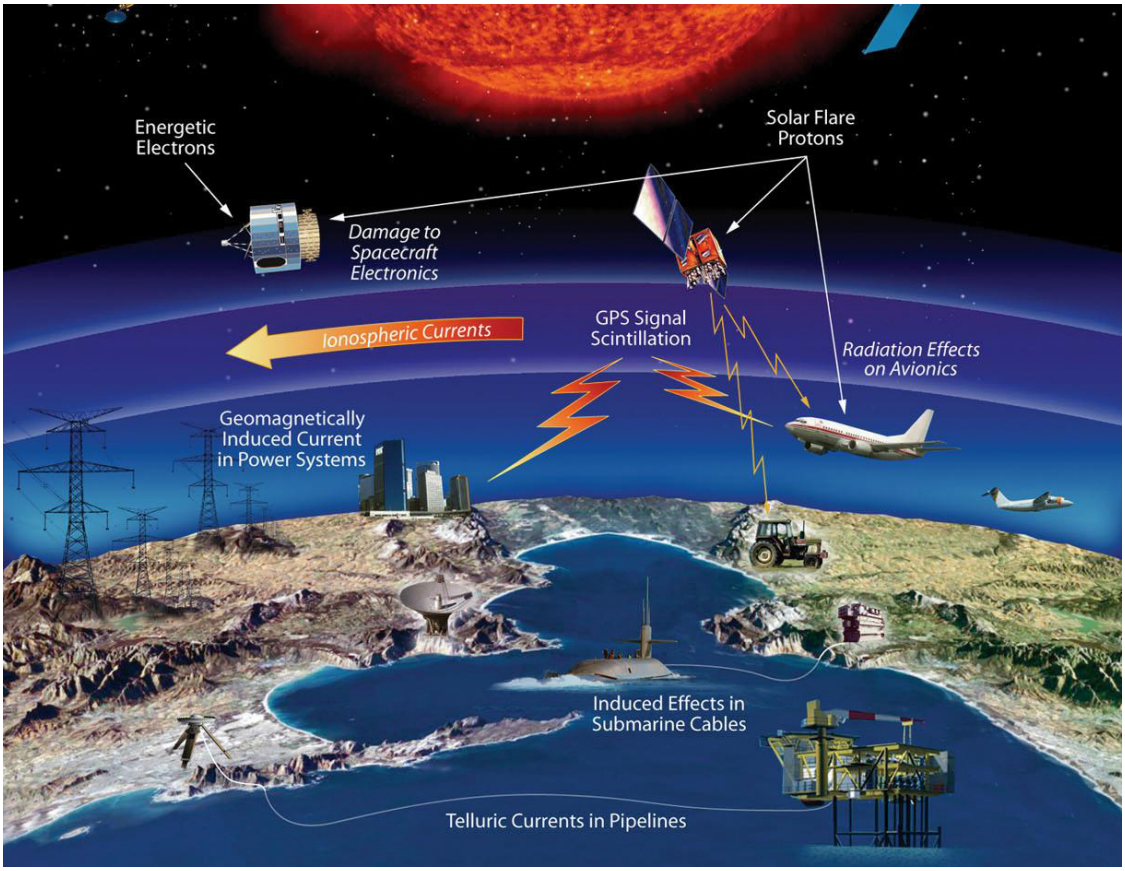

FIGURE 1.5: Space Weather effects in the ionosphere, atmosphere, and on the ground. Man-made technologies from satellites to airplanes to pipelines run the risk of being affected by space weather. courtesy of NASA

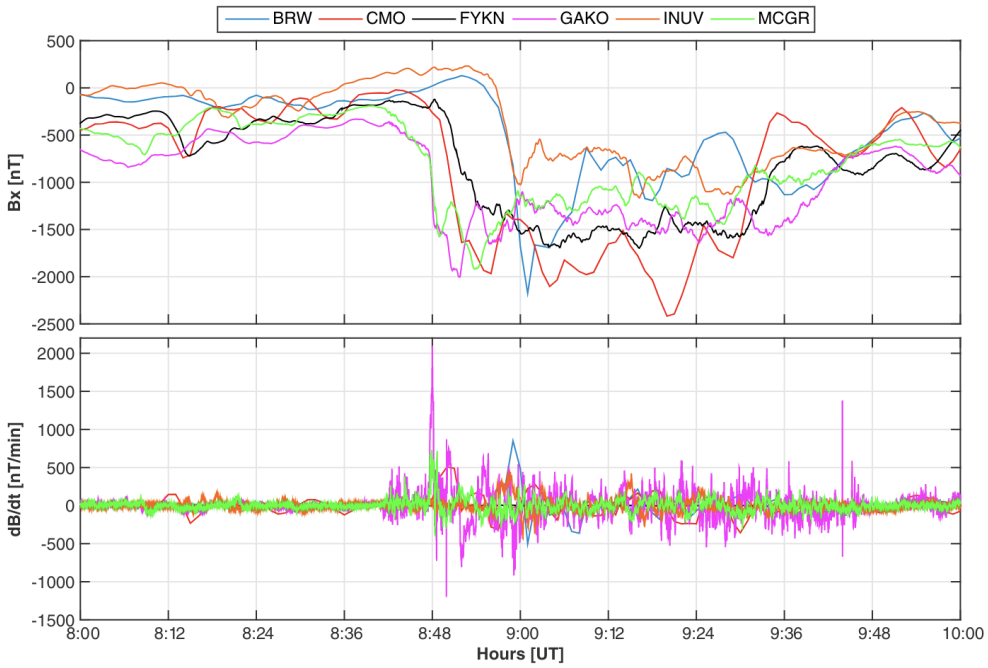

FIGURE 1.6: Example of a Localized GMD (LGMD) seen in magnetometer readings in the Alaskan sector during March 9, 2012. The top panel shows Bx for a set of magnetometers, and the bottom panel shows dB/dt for the same set. We see that dB/dt varies drastically among stations, indicating an LGMD has occurred. (Ngwira et al., 2018)

instance of this is the well-known March 1989 storm that caused the blackout of the Hydro-Quebec power grid (Boteler, 2019). In addition, because currents in the magnetosphere can close through small regions in the ionosphere, GMDs can be highly localized and of large amplitudes (Ngwira et al., 2015), which make them extremely difficult to accurately predict.

Figure 1.6 shows an example of a Localized GMD (LGMD). The bottom panel shows the dB/dt timeseries for a set of magnetometers in Alaska during March 9, 2012. The Gakona (GAKO) station records a dB/dt of almost 2000 nT/min at 8:48 UT, as opposed to the other magnetometers which measure dB/dt less than

1000 nT/min at the same time. We label this phenomenon an LGMD, because only one station in the region records such a drastic change in magnetic field.

GMDs and GICs are manifestations of Space Weather that have been studied extensively to advance our understanding of magnetosphere-ionosphere interactions and to protect our ground conducting systems (Ngwira & Pulkkinen, 2019). However, our ability to both predict these phenomena and mitigate their effects is still limited by our knowledge of the exact drivers of Localized GICs (Pulkkinen, 2015). Being able to recreate GMDs and GICs, specifically their timing and location on the ground, is crucial to advancing our ability to circumvent the effects of Space Weather.

1.2 Modeling the Magnetosphere with Magnetohydrodynamics

To study and predict the effects of the Sun on Earth's magnetic field we use ideal magnetohydrodynamic (MHD) models of the magnetosphere.

1.2.1 MHD Equations

Ideal MHD combines the fluid equations, idealized Ohm's law, and Maxwell's equations to describe the behavior of plasma in the context of a single-species charged fluid (Welling et al., 2018). Four equations provide the information needed to track the evolution of the plasma:

$$\frac{\partial \rho}{\partial t} + \nabla \cdot \left(\rho \vec{u}\right) = 0 \tag{1.1}$$

$$\frac{\partial \rho \vec{u}}{\partial t} + \nabla \cdot \left[\rho \vec{u}\vec{u} + \vec{\vec{I}}\left(P + \frac{1}{2\mu_0}B^2\right) - \frac{1}{\mu_0}\vec{B}\vec{B}\right] = 0 \tag{1.2}$$

$$\frac{\partial e}{\partial t} + \nabla \cdot \left[\vec{u}\left(e + P + \frac{1}{2\mu_0}B^2\right) - \frac{1}{\mu_0}\vec{u} \cdot \vec{B}\vec{B}\right] = 0 \tag{1.3}$$

$$\frac{\partial \vec{B}}{\partial t} + \nabla \times \left(\vec{u} \times \vec{B}\right) = 0 \tag{1.4}$$

where ρ is mass density, P is the isotropic thermal pressure, $\vec{u}$ is the bulk velocity, $\vec{B}$ is the magnetic field, and the total energy e is defined as the sum of thermal, kinetic, and magnetic energies:

$$e = \frac{P}{\gamma - 1} + \frac{\rho u^2}{2} + \frac{B^2}{2\mu_0} \tag{1.5}$$

Equation 1.1 shows conservation of mass, Equation 1.2 shows conservation of momentum, Equation 1.3 shows conservation of energy, and Equation 1.4 is the induction equation that shows the motion of the plasma relative to the magnetic field. Equation 1.4 represents the "frozen-in" flux condition, in which plasma moves along with the magnetic field.

Although ideal MHD is adequate for modeling large regions of geospace, there are aspects of MHD that do not accurately represent the dynamics of the magnetosphere and therefore do not fully reproduce the phenomena we see in reality. For example, although the frozen-in flux condition remains true for ideal MHD, this condition is violated during the process of magnetic reconnection,

resulting in a modified Equation 1.4. Because of this, reconnection occurs for numerical reasons, not physical reasons in ideal MHD. This causes the reconnection rate to be much lower than in reality, since numerical reconnection rates scale with solar wind driving (Welling et al., 2018).

1.2.2 Model Couplings

To model the geospace system, models must include ionospheric dynamics that couple to the ideal MHD equations to receive magnetospheric information and provide ionospheric feedback to the magnetospheric model. The standard method of modeling the ionosphere is to use a height-integrated electrostatic ionosphere calculated with the equation:

$$J_R = \nabla_\perp (\Sigma \cdot \nabla_\perp \Phi) \tag{1.6}$$

where J_R are FAC currents from the MHD region, Σ represents Pedersen and Hall conductances, and Φ represents the electric potential in the ionosphere. The $E \times B$ electric field calculated from the ionosphere is returned to the MHD code to determine velocity boundary conditions (Welling et al., 2018). Conductance remains the most difficult to prescribe in this type of model setup, due to the various sources of conductance and the specific knowledge of ionization rates and precipitation rates.

In addition to coupled ionospheric models, global models can include models from other regions of geospace. These additional coupled models can provide more accurate overall dynamics and better location-specific physics (Welling

et al., 2018). Kinetic ring current model coupling is one of the major improvements to global models. Others include inner magnetosphere models, which improve thermal pressure with MHD coupling.

Despite flaws in global MHD and difficulty in coupling and determining physical parameters, researchers have successfully used MHD modeling for decades to study the intricacies of the Sun-Earth system, uncover new physics, and predict space weather events. This dissertation will continue the efforts of examining global MHD and striving toward improved models.

1.3 Modeling and Prediction of GICs and LGMDs

Global MHD models coupled with other models can build a picture of geospace and the effects of the Sun on Earth from the magnetopause to the ground. Since GICs are caused by magnetic fluctuations, we can examine the changes in magnetic field (dB/dt) recorded by ground magnetometers in order to see where GICs will have the strongest impacts (Dimmock et al., 2020).

1.3.1 LMGD Modeling Challenges

Past studies of magnetometer data and spacecraft data have uncovered many of the drivers and impacts of these fluctuations (Ngwira & Pulkkinen, 2019). However, observations also show extreme localization of these GMDs, with dB/dt varying widely between magnetometers that are within approximately 100 km of each other (Dimmock et al., 2019). As a result, LGMDs prove extremely difficult to pinpoint, and observational magnetometer data is limited

by lack of coverage on the ground. In addition to analyzing observational data to learn more about the physics of LGMDs, scientists use global magnetohydrodynamic (MHD) models of the magnetosphere to reproduce the locations and strengths of magnetic field fluctuations on the ground. Ongoing efforts to study GMDs in global models include Pulkkinen et al. (2013), which presented a statistical analysis of the current ability to accurately predict GICs based on an entire set of models, magnetometer stations, and events. While literature shows that models can meaningfully reproduce and predict some GICs, the accuracy, completeness, and usefulness of these models is limited by our understanding of the underlying physics that causes GICs (and therefore LGMDs) and our ability to reproduce this physics in our models (Welling, 2019).

1.3.2 Literature Review

Researchers have studied LGMDs from many different angles. Table 1.1 presents the following information about individually identified drivers of LGMDs: Column one lists known drivers of LGMDs seen in observation; column two lists each driver's associated phenomenology; and column three lists each our capability to reproduce LGMDs caused by each driver in global MHD models. Our capability ranges from strongly able to unknown, where "Unknown" indicates that existing literature has not yet identified the phenomenon as a driver of LGMDs in global MHD models and whether or not models in their current form can reproduce the driver has not been determined.

Table 1.1 presents an overview of the current understanding of the physics of LGMDs and the capability of models to accurately represent this physics in

Drivers of LGMDs	**Phenomenology**	**Capability in Global MHD**
Bursty Bulk Flows (Wei et al., 2021)	Regional fast tail flows producing wedgelets (Birn et al., 2004)	Can reproduce (Wiltberger et al., 2015) (Garcia-Sage et al., 2015) (Eshetu et al., 2019)
Omega Bands (Apatenkov et al., 2020)	Omega-shaped auroral structure formed from regional fast flows (Vokhmyanin et al., 2021)	Unknown
Pulsating Aurora (Zou et al., 2021)	Formed from wave-particle interaction during substorms (Nishimura et al., 2020)	Unknown
Poleward Boundary Intensification (Nishimura et al., 2013)	Ionospheric manifestation of distant reconnection (Ohtani & Yoshikawa, 2016)	Can reproduce; unclear if possible locally (Blake et al., 2021)
Auroral Streamers (Nishimura et al., 2011) (Lyons et al., 2021)	Narrow auroral flow propagating toward equatorward boundary (Sergeev et al., 2004)	Unknown
Expansion of auroral bulge (Ngwira et al., 2018)	Intensification of westward electrojet due to substorm current wedge (Viljanen et al., 2006)	Can weakly reproduce (Haiducek et al., 2020) (Yang et al., 2012)

TABLE 1.1: Drivers of LGMDs identified from existing literature, each with a phenomenology and documentation of our current capability to reproduce the given driver in global MHD models.

global models. Many of the phenomena in Table 1.1 are associated with substorm signatures. Existing literature demonstrates connections between LGMDs and substorm signatures both in observation and models. On the observational side, Ngwira et al. (2018) examined spacecraft data from two events and drew a strong connection between LGMDs and multiple auroral processes that are associated with substorms. On the modeling side, scientists have used global models to explore several of the phenomena listed in Table 1.1. Substorms on the global scale have been successfully modeled by MHD simulations for some time (Lyon et al., 1998), but there are still many questions about substorms regarding timing and location of tail reconnection and other issues that have not been resolved

(Borovsky et al., 2020). Several of these use the Space Weather Modeling Framework (SWMF) (Tóth et al., 2005) and are directly related to this work. Haiducek et al. (2020) showed that the SWMF's ability to reproduce substorm signatures is statistically significant, but weak. Blake et al. (2021) explored the expansion of the equatorward boundary and used the SWMF to approximately reproduce this expansion, although they suggested higher-resolution simulations to better explore extreme events in the model.

Most relevant to this work are three papers that examine GICs in observation and in the SWMF during the September 7, 2017 event. Dimmock et al. (2019) compared GICs observed in Fennoscandia to a combination of ground conductivity models and geoelectric field models to show ground conductivity's importance on the accuracy of the model. Dimmock et al. (2020) defines useful metrics for identifying localized dB/dt occurrences, connects ionospheric processes to localized dB/dt, and emphasizes the importance of using local rather than global metrics to predict regional variability. Dimmock et al. (2021) evaluated the SWMF's ability to reproduce auroral indices and magnetic field data during the same event, and noted that higher resolution simulations performed significantly better.

A notable takeaway from these studies is that ionospheric fluctuations and substorms are significant drivers of LGMDs, and there is not a clear picture of how well global MHD models capture these phenomena on spatial scales that translate usefully to the ground. However, a high resolution, detailed comparison of model output to observation can give insight into which drivers of LGMDs are captured with global MHD models, which drivers are not captured,

and what changes we must make to our models to improve overall prediction skill.

1.4 Goals of Thesis

Understanding and prediction of LGMDs is a crucial part of protecting Earth from space weather events and building our knowledge of geospace and Sun-Earth interactions. This dissertation presents a study of the presence of Localized GMDs (LGMDs) in the Space Weather Modeling Framework (SWMF) with three goals in mind. The first goal is to determine the ability of the SWMF to reproduce observed LGMDs during storm time by examining model results thoroughly during a period of storm time. The second goal is to carefully examine different regions of the magnetosphere in the model to determine various drivers of LGMDs. The third goal is to identify the main obstacles to modeling LGMDs and present suggestions for model improvement based on identified drivers and model features.

These goals are distributed over the following chapters. Chapter 2 presents the setup of the SWMF, dissects the anatomy of the specific storm we use for the study, and defines the comparison metrics between model and observation. Chapter 3 shows a thorough data-model comparison, looking at overall model performance and then breaking the storm into distinct time periods to assess capability. Chapter 4 provides a thorough analysis of the drivers of LGMDs identified in the model and connects these drivers back to model performance and improvement capability. Finally, Chapter 5 presents a discussion on the

data-model comparison, identified LGMD drivers, and problems in the model that prevent better prediction of LGMDs. Chapter 5 concludes with ongoing questions regarding modeling LGMDs in global models, future analysis pertinent to the study, and potential improvements to the process of modeling and predicting LGMDs in global models.

Chapter 2

Event Study, Model Setup, and Metric Definition

To better explore LGMDs, we employ the Space Weather Modeling Framework (SWMF) which is currently used in the Space Weather Prediction Center (SWPC) operations. We model the period of storm time from September 6-8, 2017 and the LGMDs observed on the ground during this storm. In this section we present the circumstances of the observed event that we are modeling, describe the specific setup of the SWMF that is tailored to capture and study LGMDs, and define various metrics that we use to compare model and observation.

2.1 September 2017 Storm

We present the observed conditions of the September 2017 storm using both data from spacecraft outside the magnetosphere, and data from magnetometer stations on the ground.

2.1.1 Solar Wind Conditions

Every space weather model needs initial conditions, and in this work we use solar wind conditions during the time period of September 6-8, 2017. Figure 2.1 shows storm conditions captured by the DISCOVR spacecraft at L1, 1.5 million kilometers from Earth. This storm is of particular interest because it was a decently large Coronal Mass Ejection (CME) that was directed towards Earth and caused localized GIC activity on the ground, and also because it was characterized by a collection of different features present in the solar wind conditions. The storm began on September 6 and its effects continued through September 7 and 8. Throughout this time there were two instances of southward-turning IMF B_z, as well as two sudden storm commencements in which the solar wind speed increased by 200 km/s each time. There is evidence of substorm activity following both the first shock and the second (Clilverd et al., 2018; Dimmock et al., 2019), which will be relevant in the analysis of LGMDs throughout the storm.

2.1.2 Ground Magnetometers

On the ground, the IMAGE magnetometer network captured large magnetic fluctuations caused by this space weather event. In this study we examine a subset of the IMAGE magnetometer network in Fennoscandia. Dimmock et al. (2020) uses the same set of magnetometers grouped into Subset 1 and Subset 2. Figure 2.2 shows the geographical locations of the IMAGE magnetometer stations, with Subsets 1 and 2 marked in yellow. Subset 1 contains 4 magnetometers at latitudes from 75 to 80 degrees. Subset 2 contains 8 magnetometers

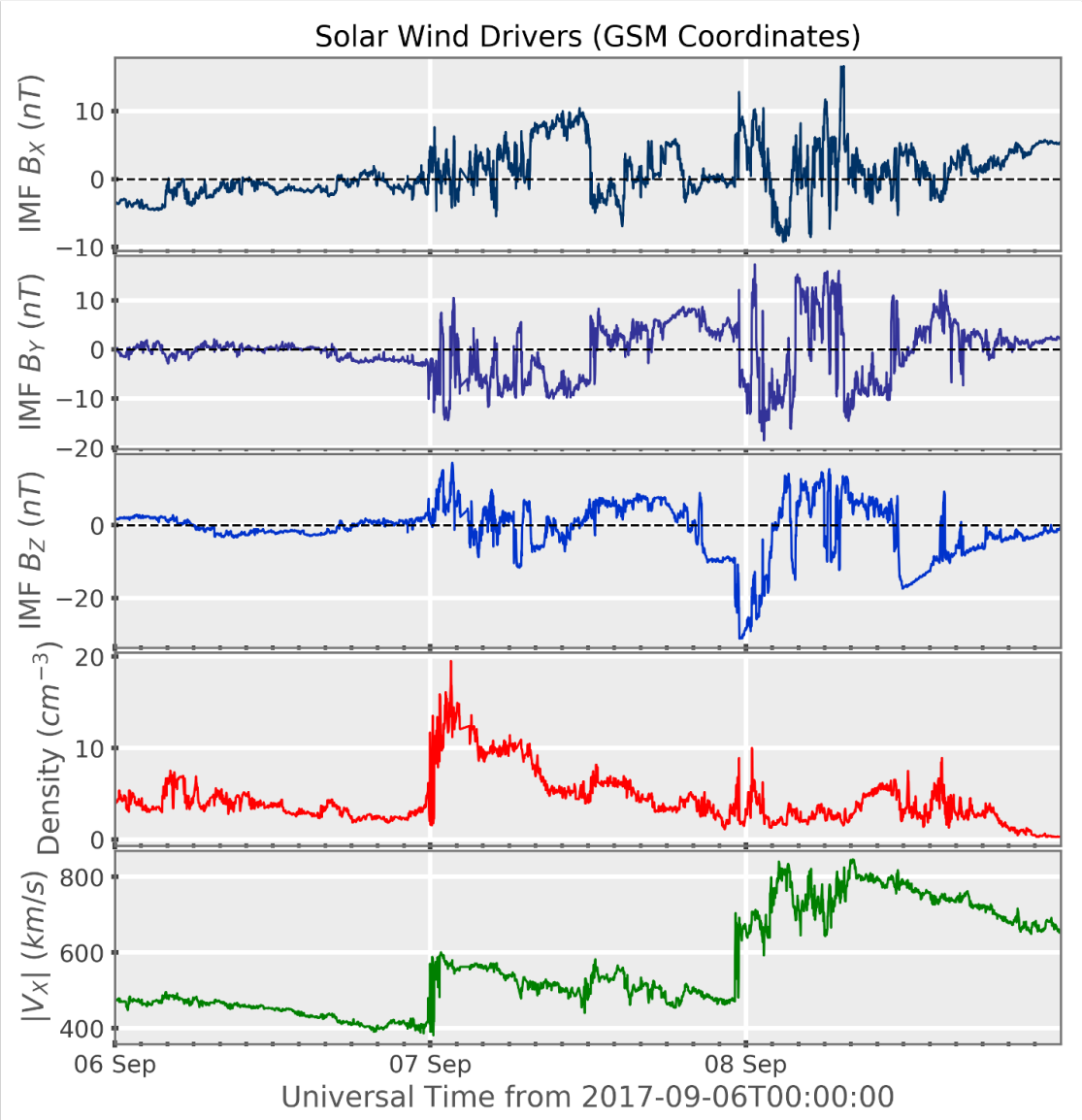

FIGURE 2.1: SWMF inputs for the September 6-8, 2017 storm. IMF, density, and solar wind speed are measured at L1.

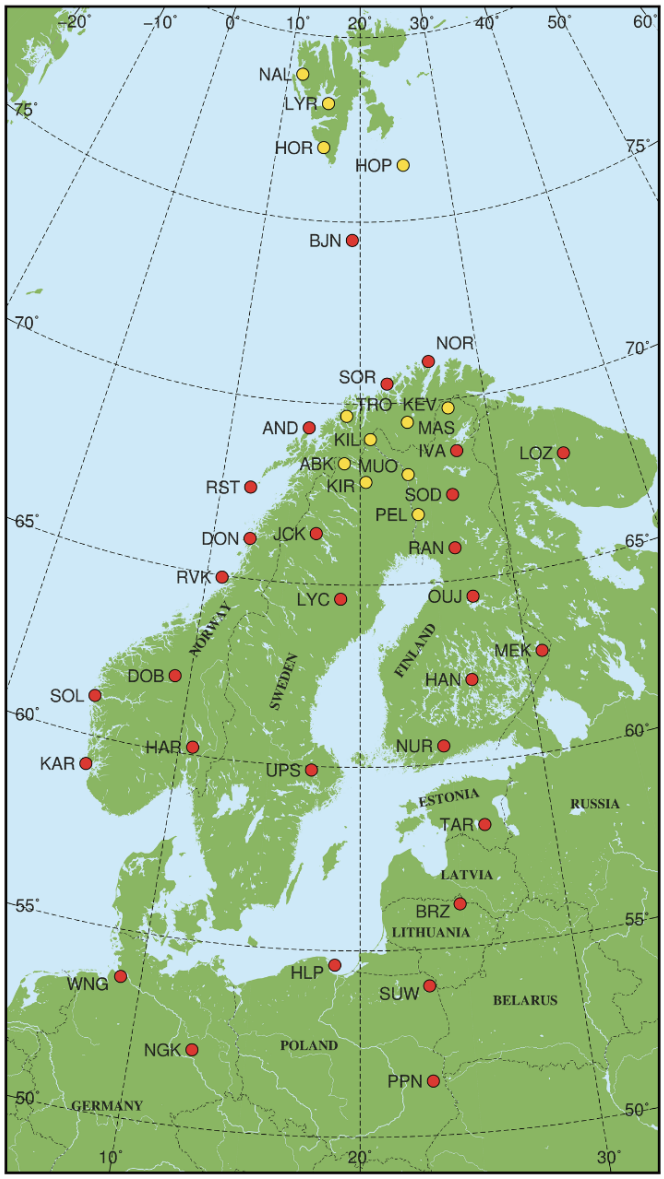

FIGURE 2.2: IMAGE magnetometer network, with Groups 1 and 2 magnetometers marked in yellow. Group 1 consists of the four magnetometers between 75 and 80 degrees latitude, and Group 2 consists of the eight magnetometers between 65 and 70 degrees latitude. (Dimmock et al., 2020)

at latitudes from 65 to 70 degrees. We use the magnetometer data from Subset 2 in this study, because although the stations sit at lower latitudes, Subset 2 contains more magnetometers and provides a more accurate picture of LGMDs throughout the event. Subset 2 magnetometers are separated from each other by approximately 100 kilometers and form a total area of approximately 500 by 200 kilometers. Table 2.1 lists the stations along with their geographical latitudes and longitudes.

Station	Code	GLat (°)	GLon (°)
Abisko	ABK	68.35	18.822
Kevo	KEV	69.76	27.07
Kilpisjärvi	KIL	69.06	20.77
Kiruna	KIR	67.84	20.42
Masi	MAS	69.46	23.07
Muonio	MUO	68.02	25.53
Pello	PEL	66.90	24.08
Tromsø	TRO	69.66	18.94

TABLE 2.1: List of stations from IMAGE magnetometer network used in this study. This list corresponds to Subset 2 from Dimmock et al. (2020) and contains stations in between 65-70 degrees latitude.

2.2 The Space Weather Modeling Framework

While there are multiple viable MHD models that have been developed over time, and even more combinations of MHD with other models, this dissertation utilizes a specific configuration of the Space Weather Modeling Framework (SWMF) (Tóth et al., 2005) to model the effects of the September 2017 storm on the magnetosphere and recreate the ground magnetic response. We describe the general setup of the model and then the specificchanges made for this study.

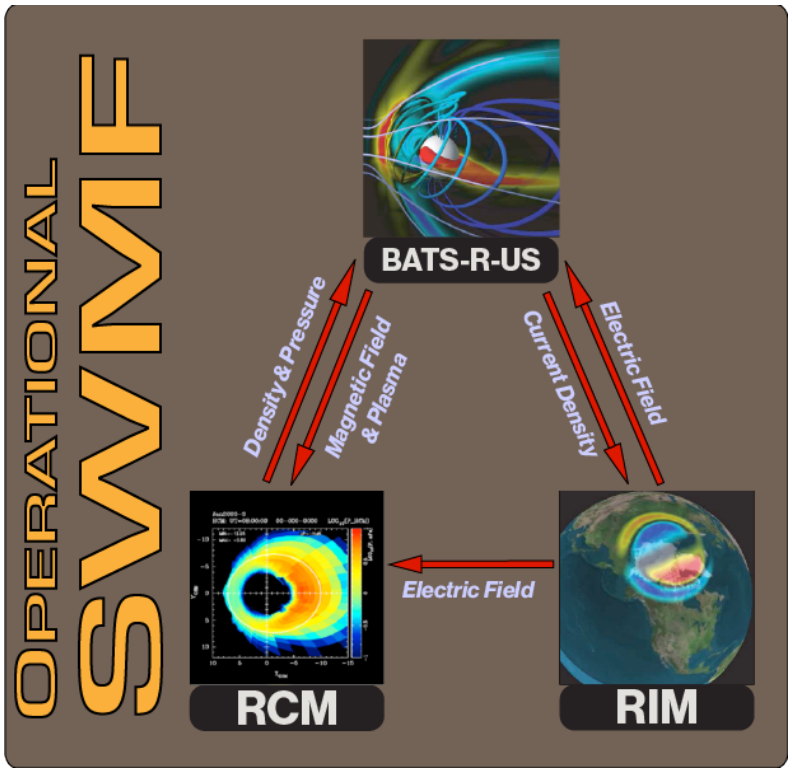

FIGURE 2.3: The Space Weather Modeling Framework setup, showing the MHD, ionosphere, and ring current coupled models along with the specifics of their couplings.

2.2.1 General Model Configuration

The SWMF is a complex system of models that couple together to describe the magnetosphere-ionosphere system. Figure 2.3 shows the three models and their couplings. The Block Adaptive Tree Solar-Wind Roe Upwind Scheme (BATS-R-US) uses ideal magnetohydrodynamic equations to model the global magnetosphere and has a block-adaptive grid that models regions of interest with higher spatial resolution (Welling & Liemohn, 2014). The Ridley Ionosphere Model (RIM) (Ridley et al., 2004) is a shell ionosphere calculated by solving 2-D Ohm's Law. The Rice Convection Model (RCM) (DeZeeuw et al., 2004) is a drift

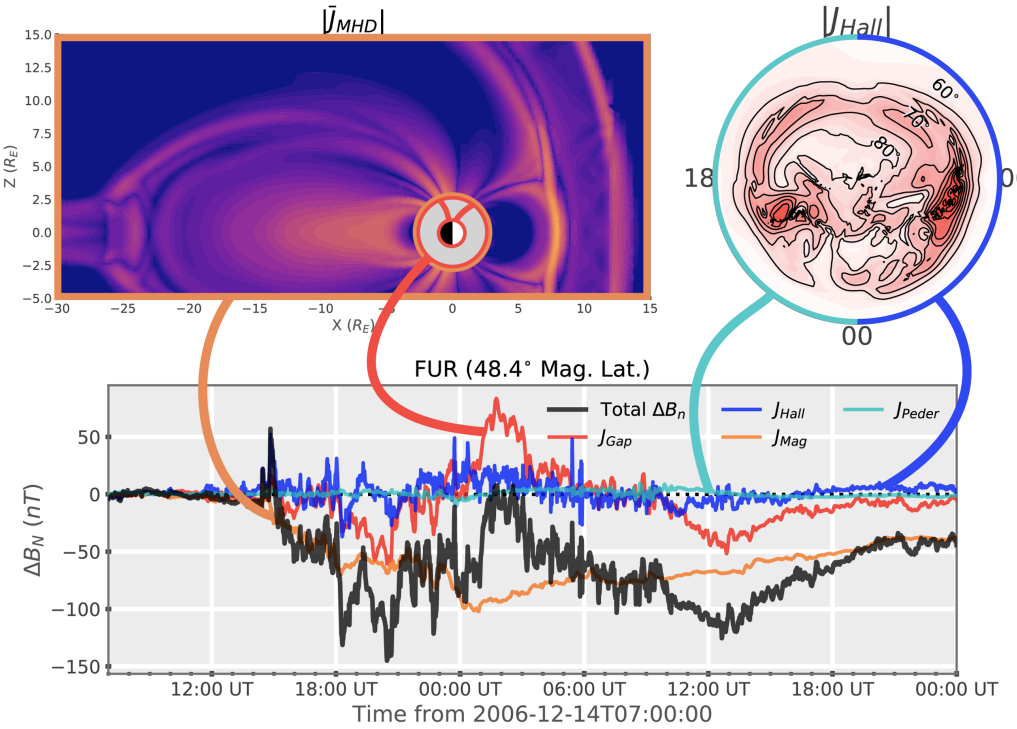

FIGURE 2.4: Biot-Savart integrals calculating virtual magnetometer readings using four different current sources - Hall currents, Pedersen currents, Field-Aligned currents, and MHD-domain currents. These four sources make up the total ΔB_N in the SWMF.

model of the inner magnetosphere. RIM provides electric field information to both RCM and BATS-R-US and receives current density from BATS-R-US. RCM provides density and pressure values to BATS-R-US and receives magnetic field and plasma information in return. As the model progresses in time, the three models run independently for small time periods, stop to exchange the variable information described above, and continue running with updated coupled values. SWMF output is a rich set of relevant magnetospheric and ionospheric variables. Output frequency used in this dissertation is one minute, but possible frequency can be less than one second.

Besides magnetosphere and ionosphere variables, the SWMF output includes a grid of virtual magnetometers that we can compare to observational magnetometer data. These virtual magnetometers use Biot-Savart integrals to calculate magnetic perturbations using four different current sources from both the ionosphere and the magnetosphere - Hall currents, Pedersen currents, Field-Aligned Currents, and currents from anywhere in the MHD region of the simulation. Figure 2.4 shows the regions that define each different current source, and a time series of the contributions from each source during the September 2017 event. These virtual magnetometers allow us to analyze conditions at the exact locations of the real magnetometers.

2.2.2 Specific Model Configuration

The Space Weather Prediction Center (SWPC) uses the SWMF for live prediction of Space Weather events, and this dissertation utilizes a configuration of the SWMF slightly modified from the operational SWPC setup. The most important modification is increased spatial resolution in the model. Dimmock et al. (2021) analyzed the effects of SWMF grid resolution on the reproduction of observed GMDs and GICs using three increasingly high-resolution grid configurations, shown in Figure 2.5. Each column shows the configuration for a different resolution with the top panel showing the distribution of the cells used and the bottom panel showing the resolution of the current density near the inner boundary. Column a shows the lowest-resolution configuration, which uses 1 million cells and a minimum 1/4 Earth Radii (R_E) spacing between cells. This is the resolution used for SWPC operations and maps to 3 degrees on the ground.

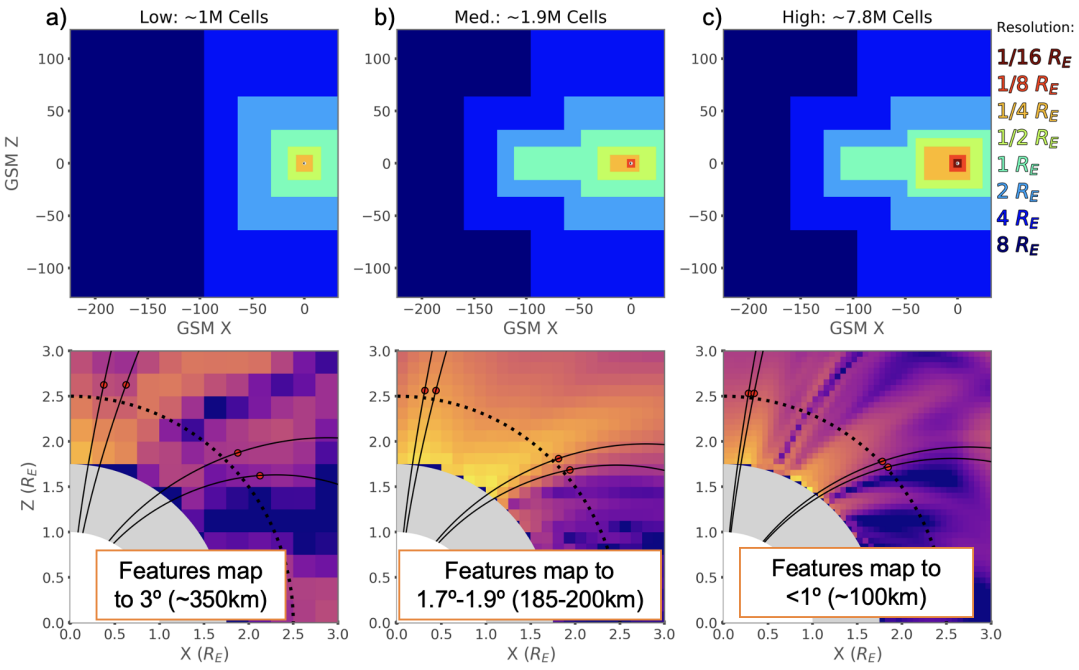

FIGURE 2.5: SWMF grid resolution for low-, medium-, and high-resolution runs. Top row shows grid configuration for each resolution. Bottom row shows feature mapping capability for each resolution. (Modified from Dimmock et al. (2021)).

Column b shows the mid-resolution configuration, which uses 1.9 million cells and a minimum 1/8 R_E spacing between cells. This configuration maps to 1.7-1.9 degrees on the ground. Column c shows the high-resolution configuration, which uses 7.8 million cells and a minimum 1/16 R_E spacing between cells. This configuration maps to less than 1 degree on the ground. Dimmock et al. (2021) found that the highest-resolution configuration most closely matched observation. This dissertation presents results using the same high-resolution configuration to capture the most detailed magnetospheric and ionospheric structure. In addition to using a high-resolution grid, this dissertation uses a configuration of the SWMF with a higher-density virtual magnetometer output than that used in SWPC operations. This provides higher-resolution GMD data that will be instrumental in studying LMGDs.

2.3 Metrics

This dissertation now shows a more detailed methodology for analyzing LGMDs in the setup of the SWMF described in the previous section. Comparing LGMDs seen in the model to those observed by real magnetometers involves calculation of metrics using the model, analysis of model outputs in different regions of geospace, and comparison of metrics and model dynamics to observed reality.

2.3.1 Region-to-Specific Difference

As a starting point, we utilize the existing metric Region-to-Specific Difference (RSD), defined in Dimmock et al. (2020), which is a metric that peaks when an LGMD is occurring for a group of magnetometers. We calculate RSD using the equation:

$$RSD_{dB/dt} = max\left(\left|\frac{dB_H}{dt} - \frac{d\overline{B_H}}{dt}\right|\right) \tag{2.1}$$

where dB_H/dt is the horizontal component of the change in magnetic field at a single station, and $d\overline{B_H}/dt$ is the average of all the stations *not including* the station from which $d\overline{B_H}/dt$ is being subtracted. Because RSD compares dB/dt recorded by a magnetometer to the average dB/dt of the other magnetometers in the set, RSD spikes when a single magnetometer yields a much different value than all the others in the set, indicating that an LGMD has occurred. We calculate the RSD for dB/dt at each 1-minute interval during the event.

In addition to calculating RSD for observational magnetometer data, we can calculate RSD for the virtual magnetometers in our model output to see how well our model can reproduce the spikes in RSD that indicate LGMDs. Section 3.2 examines RSD throughout the run both in reality and in the model.

2.3.2 New Metrics and Station Spread

RSD is an extremely useful metric on the ground, and we can extend this usefulness even further by calculating the RSD metric in other regions of geospace. In the SWMF, BATS-R-US uses ray tracing to map magnetic field lines from the

ground, through the ionosphere, and into the magnetosphere. We can use this ray tracing to examine the conditions anywhere along the field lines that originate from magnetometer locations on the ground. This allows us to differentiate between ionospheric and magnetospheric sources of ground perturbations. We calculate RSD_{iono} and RSD_{tail} using equations similar to Equation 2.1:

$$RSD_{iono} = max\left(\left|X_{iono} - \overline{X}_{iono}\right|\right) \tag{2.2}$$

$$RSD_{tail} = max\left(\left|X_{tail} - \overline{X}_{tail}\right|\right) \tag{2.3}$$

where in this case, X_{iono} represents any relevant variable from the model ionosphere output, and X_{tail} represents any relevant variable from the model magnetosphere output. Section 3.5 presents relevant variables in both the ionosphere and magnetosphere, and calculates RSD for these variables.

Following the station locations along field lines also allows us to track how far apart the field lines spread apart from each other as they reach the equatorial plane. Figure 2.6 shows x and y coordinates of the points originating from virtual magnetometers on the ground and mapping along field lines to the Z=0 plane. Throughout the event, there are periods during which the x and y coordinates of each station move almost in unison, and periods of time where x or y differs among the set of station footpoints. We call this separation of the field lines "station spread."

We can quantify the amount of station spread at any given epoch by subtracting the minimum distance between stations from the maximum. This will

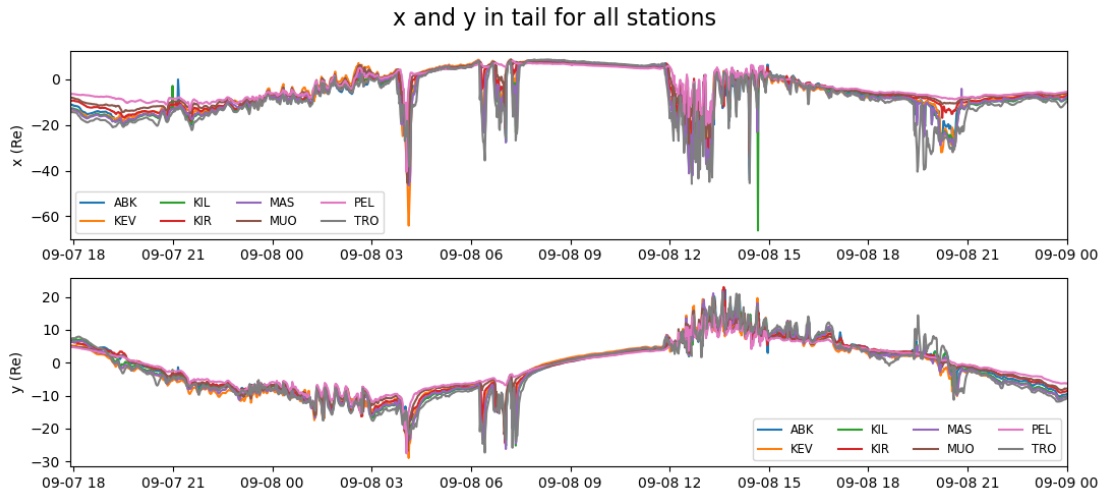

FIGURE 2.6: X and Y coordinates for all footpoints in the magnetosphere that map to magnetometer stations. Throughout the September 2017 event we note several locations where the mapped station locations are very far apart.

create a timeseries with peaks at any epoch where the stations are spread apart. We will use this method of quantifying station spread in Section 3.5. The existence of station spread indicates that larger dynamics in the magnetosphere can map down to small locations on the ground, meaning that all LGMDs in the model are not necessarily caused by small spatial-scale structure.

Chapter 3

SWMF Model-Observation Comparison

This chapter uses the model setup, event, and metrics defined in Chapter 2 to quantify SWMF performance over the September 2017 event. We examine overall storm dynamics in model and observation, discuss "hit" and "miss" rates for reproducing LGMDs, compare RSD on the ground, show outcomes of changing the grid resolution of the model, and calculate RSD_{iono} and RSD_{tail} in the model.

3.1 Storm Dynamics

Section 2.1 details the solar activity and the solar wind conditions associated with the September 2017 storm. We can use Dst and SYM-H calculated both from the model and from observation to assess the overall performance of the run compared to the behavior of the same indices in observed reality. Figure 3.1 shows observed Dst in orange, modeled Dst in blue, observed SYM-H in green, and modeled dynamic pressure in red. The model captures the dynamics

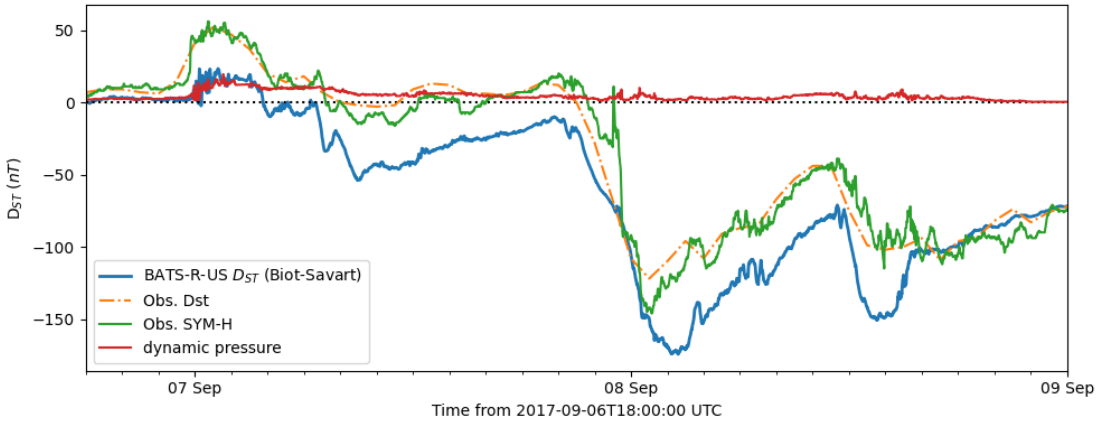

FIGURE 3.1: Comparison between SWMF Dst/dynamic pressure and observed Dst/SYM-H. The SWMF captures overall storm dynamics well, with a slight offset. There is an hour-long time shift between model and observation that explains the shift between model and observational RSD comparison.

of the storm accurately on the global scale. There is a slight offset between the magnitude of observed and modeled Dst, and the initial Dst jump in the model is smaller in magnitude, but the general structure of the storm is represented in the model. The two shocks around September 7 00:00 UT and September 8 00:00 UT correspond to the spikes in solar wind speed observed at the same times in Figure 2.1.

Note that the initial jumps in modeled Dst and dynamic pressure occur approximately an hour after the observed jump in Dst. This indicates that despite the SWMF producing the correct output from given data, the solar wind upstream data at the magnetosheath has changed since moving from L1, where they were initially captured by DISCOVR. This kind of effect is a known factor in model analysis (Morley et al., 2018). This time delay propagates through the model and will be noted in all other data-model comparisons. In addition to the

time delay, note that this difference between L1 and magnetosheath data could manifest as additional uncertainty in our results.

3.2 RSD On the Ground

Section 2.3 introduced the metric RSD as a tool for identifying LGMDs in model and observation. We now calculate RSD for the entire September 2017 event and compare observational and model results to quantify the performance of the SWMF in identifying LGMDs. Figure 3.2 shows RSD in three different contexts, comparing model and observational RSD in the first two panels and showing a breakdown of the sources of modeled RSD in the third panel. Figure 3.2a shows RSD calculated for virtual magnetometer stations in red and RSD calculated for real-world magnetometer readings in grey. We can note several things from this initial comparison of observed versus modeled RSD. First, the model captures activity in the first half of the event, from September 7, 23:00 UTC to September 8, 03:00 UTC, but fails to capture the RSD spikes between September 8, 15:00 UTC to September 8, 22:00 UTC in the second half of the run. Second, the model does not reproduce RSD spikes with the same magnitude as observation. The observed spikes with the highest amplitudes reach up to nearly 50 nT/s, whereas the modeled RSD spikes hit their top amplitude at nearly 20 nT/s. Third, we see that the background RSD for the model matches fairly well with observation in the unscaled version on the comparison, but when model results are scaled to observation as in Figure 3.2b, the background amplitudes are higher than observed RSD. We also note that Figure 3.2b shows

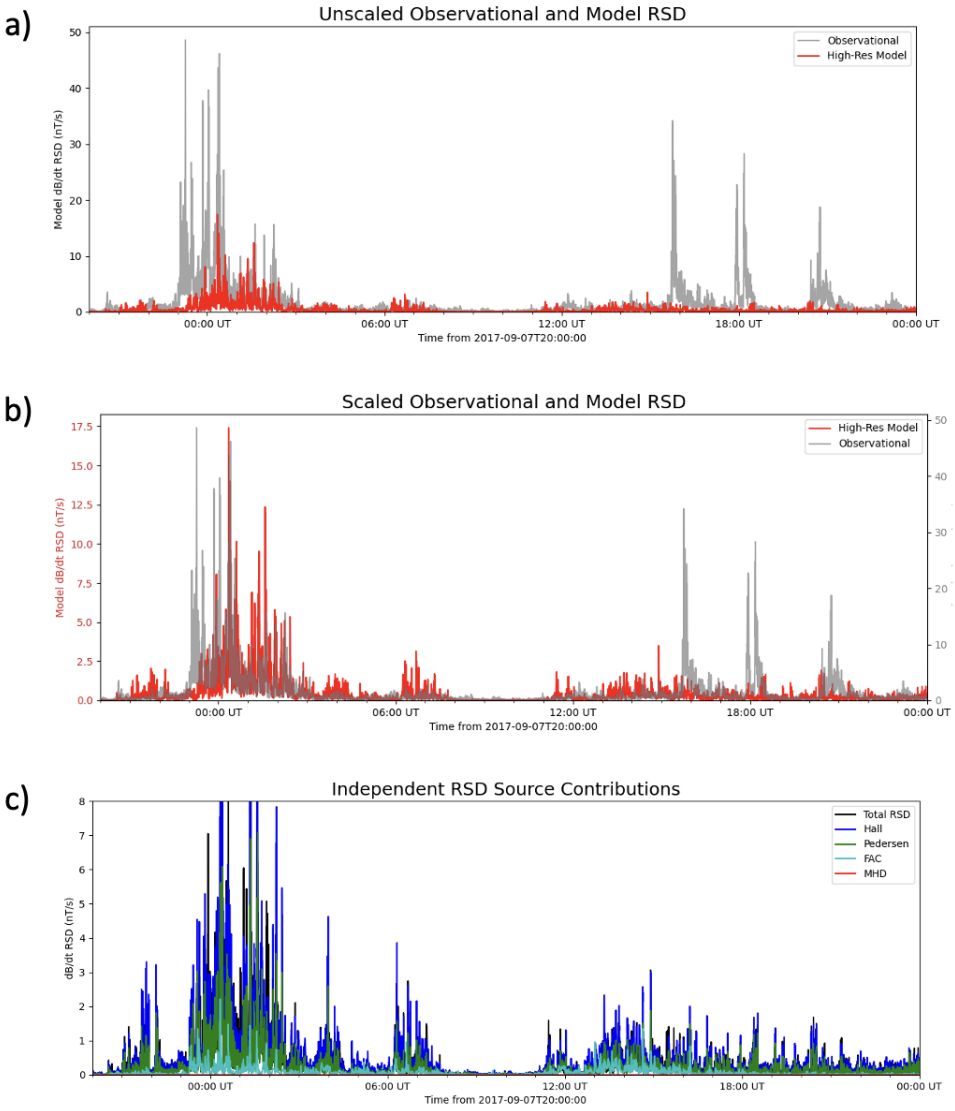

FIGURE 3.2: Region-to-Specific Difference (RSD) for the entire September 2017 event, calculated for both observation and model. Panel a shows the comparison between model and observational data with both on the same scale. Panel b shows the comparison between model and observational data, with model RSD scaled to the observational data. In both a and b, RSD calculated from IMAGE magnetometer station data is in gray, and RSD calculated from the SWMF virtual magnetometer output is shown in red. Panel c shows the breakdown of each current source from the model used in Biot-Savart integrals to calculate dB/dt RSD.

the effects of the time shift between model and observation seen in Figure 3.1. When the model results are scaled to match observation, we see the strongest model RSD peaks centered around September 8, 00:30 UT appearing approximately 1.5 hours after the strongest observed peaks in RSD, which matches the time shift seen in Figure 3.1.

In Figure 3.2c, we break down the modeled dB/dt RSD by contribution from each Biot-Savart integral source to get indicators about the potential drivers of LGMDs (Welling, 2019). Black indicates the total RSD, blue indicates Hall current contributions, green represents Pedersen current contributions, cyan represents FAC contributions, and red represents MHD current contributions. We see that the Hall currents contribute most to the total, Pedersen and FAC contribute moderate amounts, and the MHD current contribution is negligible. This provides an initial indication of what regions are most important to driving RSD spikes in the model.

3.3 Statistics

We can quantify the number of LGMDs thoughout the storm by defining thresholds for dB/dt that indicate the presence of small, mid-size, and large LGMDs both in observation and in the model.

3.3.1 Percentiles

We define the size of an LGMD based on the highest threshold RSD passes before receding below the lowest threshold. To determine which thresholds are

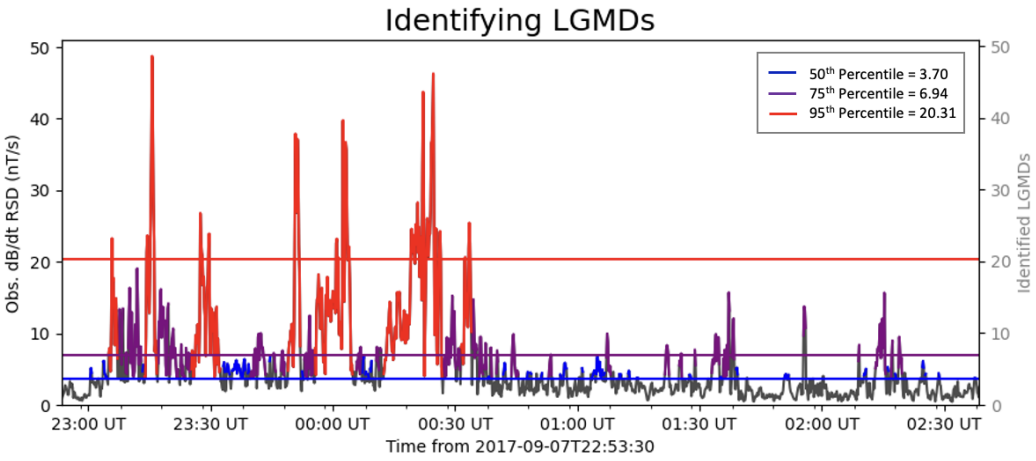

FIGURE 3.3: Observed RSD from September 7, 23:00 UT to September 8, 02:30 UT shown with thresholds calculated using 50th, 75th, and 95th percentiles over this time period.

relevant and how model and observation compare, we calculate 50th, 75th, and 95th percentiles for model and observation.

Figure 3.3 shows observed RSD in the period of storm time from September 7, 23:00 UT to September 8, 02:30 UT with blue indicating 50th percentile LGMDs, purple indicating 75th percentile LGMDs, and red indicating 95th percentile LGMDs. Blue, purple, and red horizontal lines represent the thresholds for 50th, 75th, and 95th percentiles respectively. Figure 3.4 shows the same statistics for percentiles calculated from modeled RSD during the same time period. Note that over the same time period, LGMDs in observation occur earlier in time than modeled LGMDs, which is consistent with the time shift between model and observation.

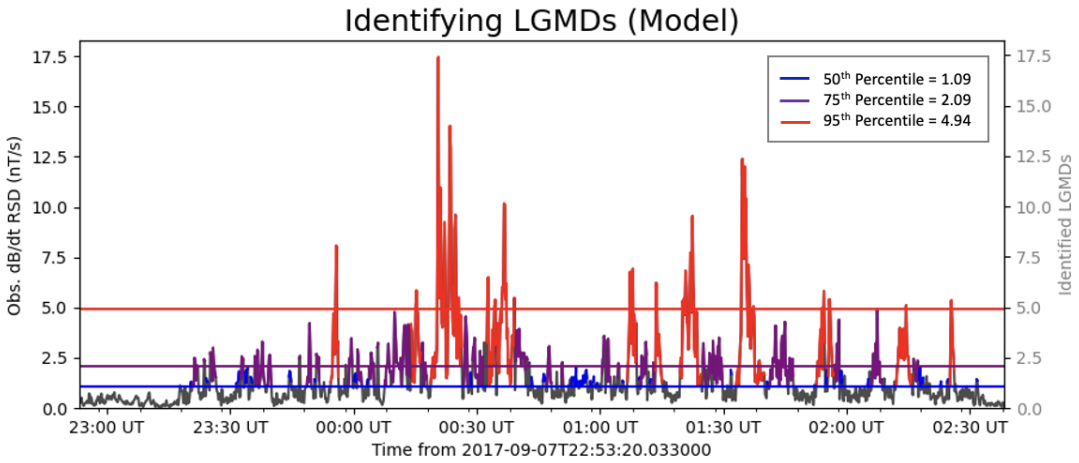

FIGURE 3.4: Modeled RSD from September 7, 23:00 UT to September 8, 02:30 UT shown with thresholds calculated using 50th, 75th, and 95th percentiles over this time period.

Percentile	Threshold (nT/s)		Number of LGMDs	
	Observed	Modeled	Observed	Modeled
50th	3.70	1.09	105	160
75th	6.94	2.09	51	52
95th	20.31	4.94	10	13

TABLE 3.1: Thresholds based on observed and modeled percentile calculations and number of LGMDs recorded crossing each threshold.

Table 3.1 shows each percentile with the thresholds calculated for modeled and observed RSD, as well as the number of LGMDs in model and observation for each threshold. 50th percentile produces 105 observed and 160 modeled LGMDs, 75th percentile produces 51 observed and 52 modeled LGMDs, and

95th percentile produces 10 observed and 13 modeled LGMDs. The 95th percentile LGMDs are the most important since they have the highest magnitudes, and we see nearly the same number of modeled and observational LGMDs in this row and in the 75th percentile row. This is a good indication that with proper scaling and time shifting, model and observation see a similar number of high-amplitude LGMDs.

3.3.2 Binary Event Tables

Although the model and observational thresholds are very different for the 95th percentile (20.31 for observation and 4.94 for model), we can get a general idea of the model performance by creating binary event tables to document overlap in LGMDs between model and observation. A binary event table examines a small time window and determines whether the model RSD crossed a certain threshold, and whether observational RSD crossed the same threshold. There are four outcomes to this comparison, and a binary event table keeps track of how many time intervals end in each outcome. These four outcomes are Hits, Misses, False Alarms, and True Negatives. The outcome registers as a Hit when an LGMD appears in both model and observation, and a Miss when an LGMD appears in observation but not in the model. A False Alarm indicates time windows during which an LGMD appears in the model but not observation, and finally, the outcome is a True Negative when an LGMD appears in neither model nor observation.

Modeled?	Observed?	
	Yes	No
Yes	12	2
No	11	7
Total LGMDs		32

TABLE 3.2: Binary event table for a threshold of 5 nT/s and a time interval of 300 seconds. Under these conditions, the model yielded a Hit Rate of 0.522, a False Alarm Rate of 0.222, and a Heidke Skill Score of 0.230.

Table 3.2 shows the Hits, Misses, False Alarms, and True Negatives during the period of activity seen in Figures 3.3 and 3.4. These binary event tables were calculated using a threshold of 5 nT/s, which is the 95th percentile threshold for modeled RSD. Because the model is time-shifted, the model RSD used in the calculation of this binary event table begins on September 8, 00:16 UT, whereas the RSD used from observation begins at September 7, 23:00, which is one hour and sixteen minutes earlier than the modeled RSD period. This accounts for the time shift and matches the model more accurately with observation. This specific configuration yields 12 Hits, 11 misses, 2 False Alarms, and 7 True Negatives.

From this information we can calculate the Hit Rate, False Alarm Rate, and Heidke Skill Score. Hit Rate shows what percentage of the total observed LGMDs were captured in the model, which in this case was 52.2%. False Alarm Rate shows what percentage of the total number of LGMDs were only in the model and not observed in reality, which in this case was 22.2%. Heidke Skill Score determines the prediction skill of a model compared to random chance and ranges

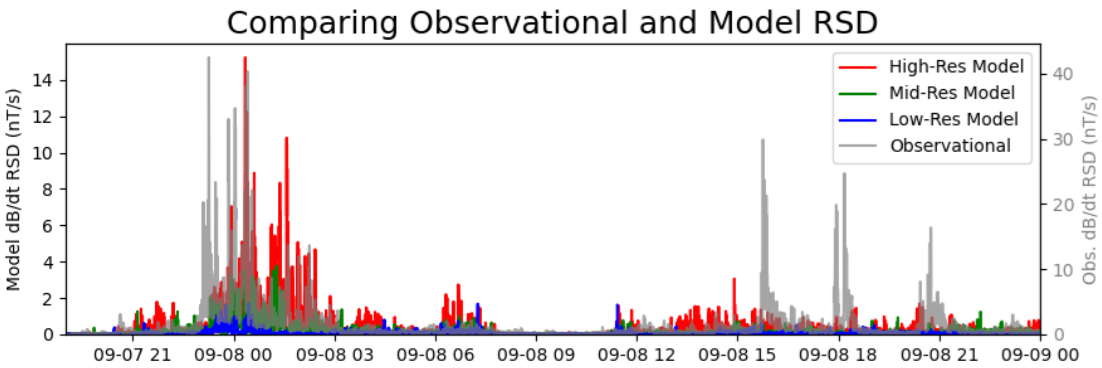

FIGURE 3.5: RSD calculated for high, mid, and low grid resolutions used to run the SWMF. High-resolution (7.8 million cells) is shown in red, mid-resolution (1.9 million cells) in green, and low-resolution (1 million cells) in blue.

from $-\inf$ to 1, where 1 is a perfect score. The Heidke Skill Score is 0.230 for the specific threshold of 5 nT/s, time window of 300 seconds, and overall time period of 3.5 hours.

3.4 Grid Resolution

Returning to the three different grid resolutions discussed in Section 2.2, we calculate dB/dt RSD for each of these configurations. Figure 3.5 shows the observational RSD in grey, high-resolution model RSD in red, mid-resolution model RSD in green, and low-resolution model RSD in blue. It is very apparent that the model RSD performance greatly improves with increased resolution, which is consistent with the results of Dimmock et al. (2021) which showed improvement in model reproduction of GICs at higher grid resolutions.

3.5 Ionosphere RSD, Tail RSD, and Station Spread

We defined RSD_{iono}, RSD_{tail} and station spread in Chapter 2 and we can now quantify the capability of the SWMF to reproduce LGMDs using these additional metrics.

3.5.1 Relevant Variables

Using Equations 2.3 we will calculate RSD_{iono} for horizontal currents and RSD_{tail} for vorticity. Horizontal currents, consisting of the Hall and Pedersen currents, are relevant because they are the top contributors to the modeled RSD seen in the breakdown in Figure 3.2. We extract the horizontal currents in the ionosphere at the locations of the magnetometer stations mapped along field lines and calculate Horizontal Currents (J_ϕ) RSD_{iono}:

$$J_\phi \; RSD_{iono} = max\left(\left|J_\phi - \bar{J}_\phi\right|\right) \tag{3.1}$$

Vorticity in the tail is important because it can provide information about the field-aligned currents in the ionosphere, which are the third contributor to the RSD source breakdown in Figure 3.2. Because of the frozen-in flux theorem, we can use the equation $\mu_0 J = \nabla \times \vec{B} \propto \nabla \times \vec{u}$ to relate the curl of the magnetic field to the vorticity, which is the curl of the velocity. So, to examine how the field-aligned currents are related to LGMDs, we extract the vorticity in the equatorial plane at the mapped field line locations to calculate Vorticity (ω) RSD_{tail}:

$$\omega \; RSD_{tail} = max\left(\left|\omega_{tail} - \overline{\omega}_{tail}\right|\right) \tag{3.2}$$

3.5.2 RSD Throughout the Model Domain

We now compare RSD_{tail} and RSD_{iono} throughout the storm to $\text{RSD}_{dB/dt}$ on the ground to quantify SWMF capability to reproduce LGMDs and gain insight into which ionospheric and magnetospheric sources drive which LGMDs in the model. Figure 3.6 shows the comparison among these metrics in different regions of the simulation over the entire event. The overall behavior of RSD in horizontal currents and vorticity is marked by periods of activity coinciding with the Dst drops in Figure 3.1 around September 8, 00:00 UT and September 8, 12:00 UT. Note that 3.6a compares model and observation, so the time shift discussed in the methodology is present in this comparison. Figures 3.6b, 3.6c, and 3.6d compare model values only, so there is no time shift present in these plots.

Figure 3.6a shows modeled and observed RSD for dB/dt on the ground, with observed RSD in grey and modeled RSD in red and scaled to match observed RSD as in Figure 3.2b. Figure 3.6b shows modeled dB/dt RSD in red and J_ϕ RSD_{iono} in green. Here we see strong correlation between J_ϕ RSD_{iono} and RSD on the ground in the first half of the run. In the second half, we see J_ϕ RSD_{iono} peaks that do not correlate to any RSD activity on the ground. Figure 3.6c shows modeled dB/dt RSD in red and ω RSD_{tail} in blue. We see some correlation with RSD on the ground in the first part of the run, and much like Figure 3.6b, we see ω RSD_{tail} activity in the second half of the run that does not correspond to RSD on the ground. Figure 3.6d shows modeled dB/dt RSD in red and station spread ($R_{max} - R_{min}$) in black. Unlike J_ϕ RSD_{iono} and ω RSD_{tail}, there is no station spread in the first part of the run. However in the second part of the run,

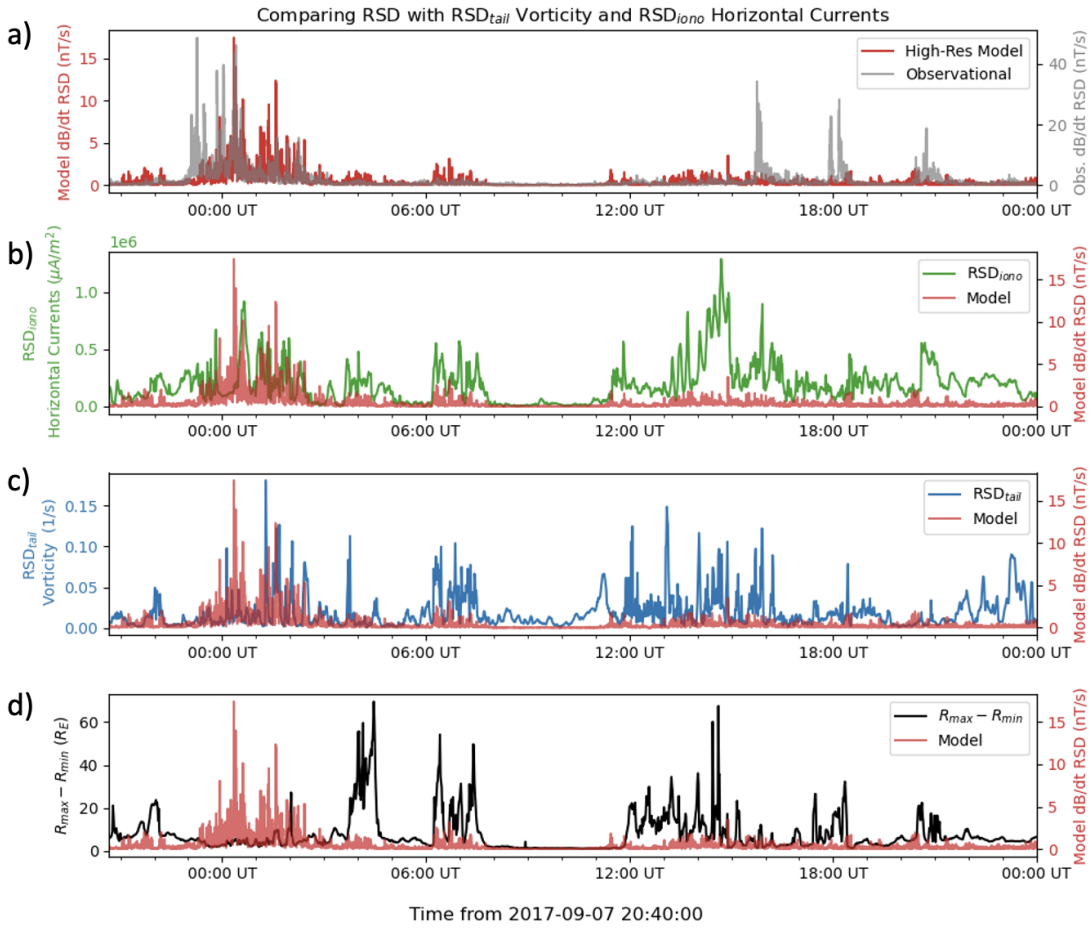

FIGURE 3.6: Comparing model RSD to four different values and metrics. Panel a) compares model RSD to observational RSD, panel b) compares model RSD to RSD$_{iono}$ calculated for horizontal currents in the ionosphere, panel c) compares model RSD to RSD$_{tail}$ calculated for vorticity in the equatorial plane, and panel d) compares model RSD to "station spread," calculated using $R_{max} - R_{min}$.

station spread correlates with both J_ϕ RSD_{iono} and ω RSD_{tail}. Examining the observational RSD in Figure 3.6a, the three spikes in the second half of the run are not reproduced clearly in any of the additional metrics.

We have thoroughly examined the behavior of the SWMF over the September 2017 storm. Overall storm-time indices indicate a time shift that we continue to address in our analysis. We have used RSD from Dimmock et al. (2020) to show more details about the sources of magnetic perturbations in the model. We have examined percentiles of a portion of the model to further compare the results to observation. We confirmed the importance of high-resolution simulations to reproduce LGMDs. Finally, we have expanded the use of RSD to other regions of the model domain. We can now transition into analysis of potential drivers of LGMDs in the model.

Chapter 4

Identifying Drivers

This chapter is devoted to determining drivers of different periods of LGMDs in the SWMF using different features in the model and more closely examining the metrics defined in Chapter 2.

4.1 Breaking Down the Storm

To explore drivers of individual LGMDs, we examine two shorter time periods within the September 2017 event. Part A of the event covers September 7, 22:00 UTC through September 8, 10:00 UTC, and Part B covers September 8, 13:00 UTC through September 9, 00:00 UTC.

4.1.1 LGMDs in Part A

We examine metrics and period of time from September 7, 22:00 UTC through September 8, 10:00 UTC Figure 4.1 is similar to Figure 3.6 but only shows Part A of the event. Part A is characterized by a period of clear correlation between dB/dt RSD spikes in the model and in observation from September 7, 23:00 UTC

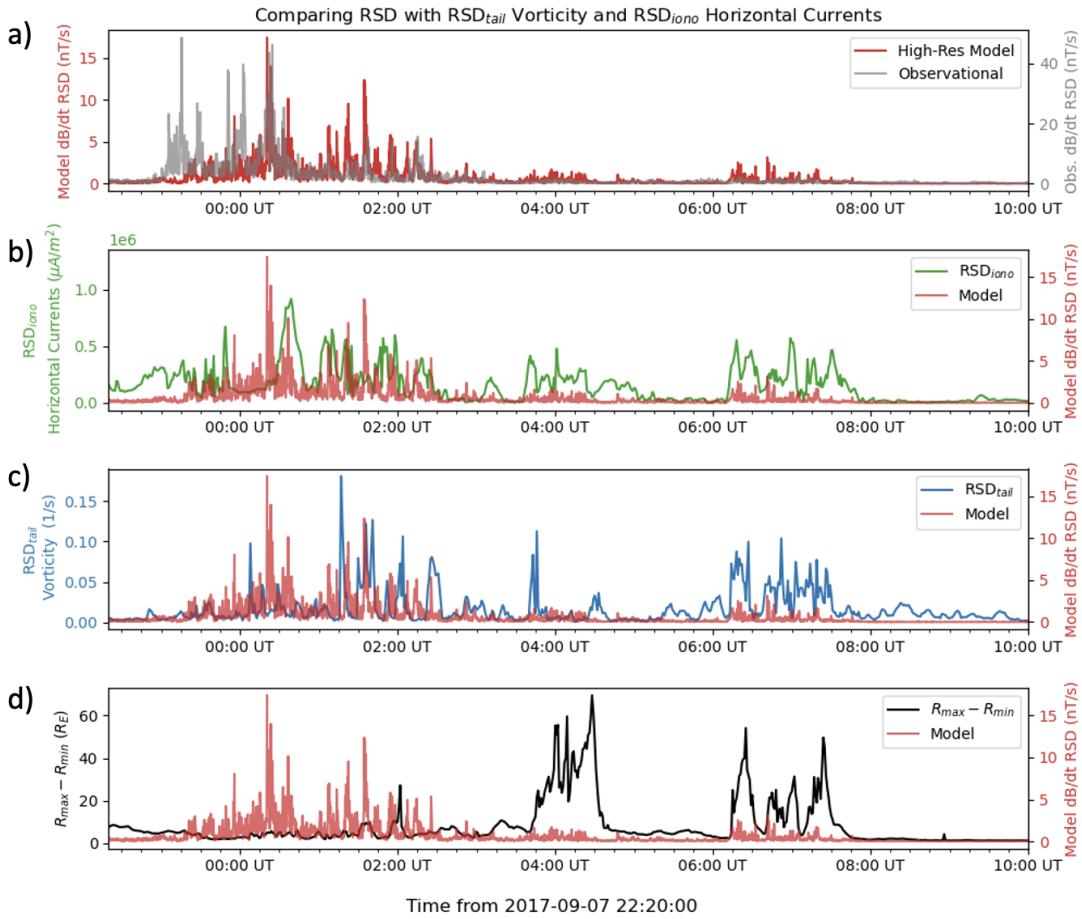

FIGURE 4.1: Part A of the September 2017 event showing September 7, 22:00 UTC to September 8, 10:00 UTC. We see a closer view of the correlation between modeled RSD on the ground, RSD$_{iono}$, and RSD$_{tail}$ in the main part of the storm.

to September 8, 03:00 UTC, seen in Figure 4.1a. Figures 4.1b-d show comparisons between the modeled dB/dt RSD on the ground and the modeled RSD calculated in other regions of the simulation. In Figure 4.1b we see strong correlation between modeled RSD and J_ϕ RSD$_{iono}$, especially for peaks in between September 8, 00:00 and 02:00 UT. In Figure 4.1c we note some correlation between modeled dB/dt RSD and ω RSD$_{tail}$, with the best correlation between September 8, 01:00 and 02:00 UT. In 4.1d we see little to no station spread in the region of large RSD spikes; however, between September 8, 03:00 UTC and September 8, 08:00 UTC we see two distinct regions of station spread corresponding to peaks in both J_ϕ RSD$_{iono}$ and ω RSD$_{tail}$ with very slight peaks in the modeled RSD on the ground, but no activity recorded in observational RSD on the ground. Despite the lack of observational response at the exact magnetometer station locations, these peaks of high station spread that correlate to other activity throughout the model indicate periods of time during which large-scale structures map down to small spatial regions of the ionosphere, indicating that large-scale phenomena in the magnetosphere can drive LGMDs on the ground.

4.1.2 LGMDs in Part B

Figure 4.2 shows Part B of the event. During this period of time we focus in on the three prominent spikes in observed dB/dt RSD, none of which are reproduced in the model RSD on the ground shown in Figure 4.2a. Taking into account the time shift between observation and model and comparing the observed RSD to the horizontal currents, vorticity, and station spread shown in

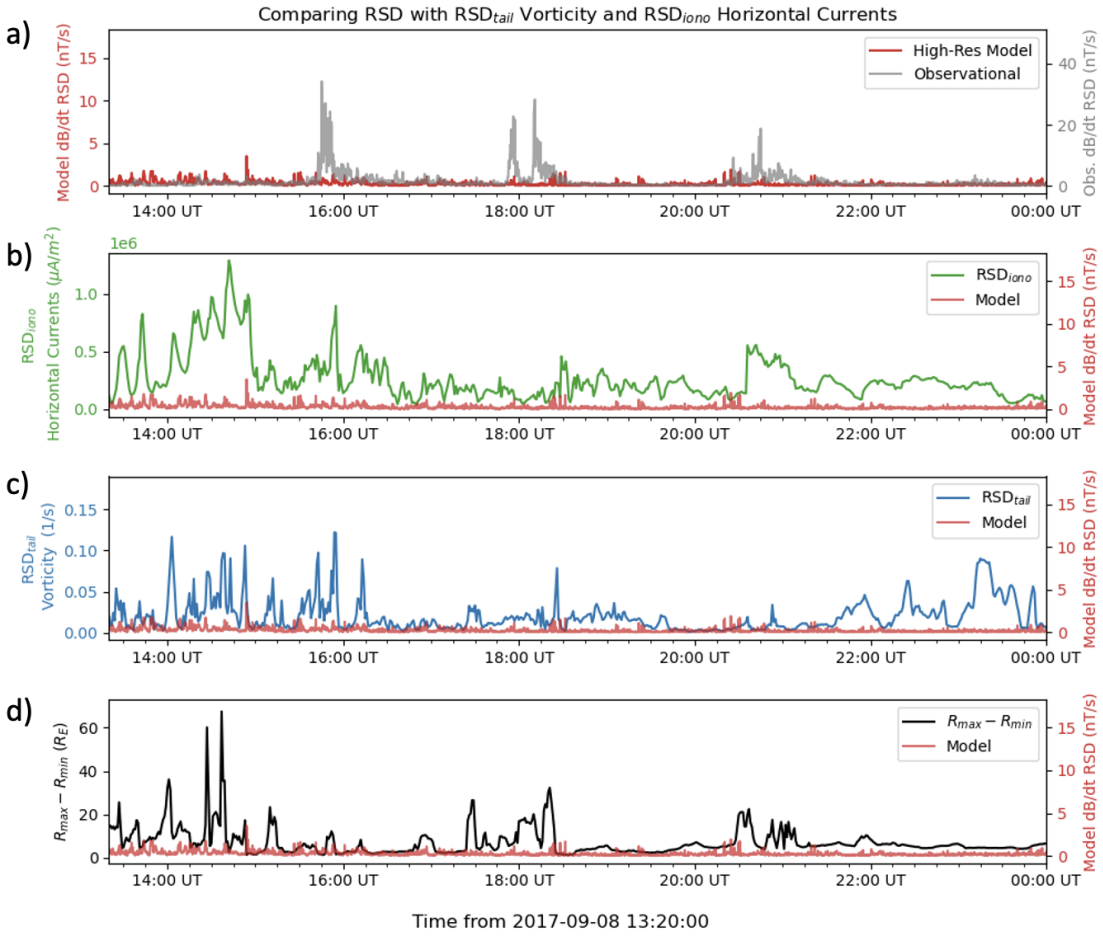

FIGURE 4.2: Part B of the September 2017 event showing September 8, 13:00 UTC through September 9, 00:00 UTC. Part B shows the three RSD peaks associated with substorm activity, and only very faint correlations with J_ϕ RSD$_{iono}$, ω RSD$_{tail}$, and station spread.

4.2B, 4.2C, and 4.2D respectively, we see some correlation with horizontal currents, faint correlation with vorticity, and clear correlation with station spread for two out of the three spikes.

4.2 Dayside and Nightside Comparisons

Examining the location of the stations relative to the Sun as Earth rotates can provide additional context about possible drivers of LGMDs. In Figure 4.3 we see the overlay of station position through Part A of the storm. The stations are located on the nightside though the first period of RSD enhancement on the ground and in both the ionosphere and magnetosphere. We see J_ϕ RSD$_{iono}$ and ω RSD$_{tail}$ activity during the nightside, but little station spread. During the dayside we see little RSD activity on the ground in either observation or model, but again we see the two periods of activity in J_ϕ RSD$_{iono}$, ω RSD$_{tail}$, and station spread.

Figure 4.4 shows Part B of the storm with the locations of magnetometer stations divided by dayside and nightside. Again we see no RSD until the stations reach the dusk region between dayside and nightside, directly after which we see the first of the three RSD spikes in observation. Similar to Figure 4.3, during the dayside we see little RSD activity on the ground in either observation or model but we do see a region of enhanced J_ϕ RSD$_{iono}$, ω RSD$_{tail}$, and station spread. On the nightside, there is some activity in J_ϕ RSD$_{iono}$, ω RSD$_{tail}$, and station spread.

A trend we can explore further is the difference between station spread on

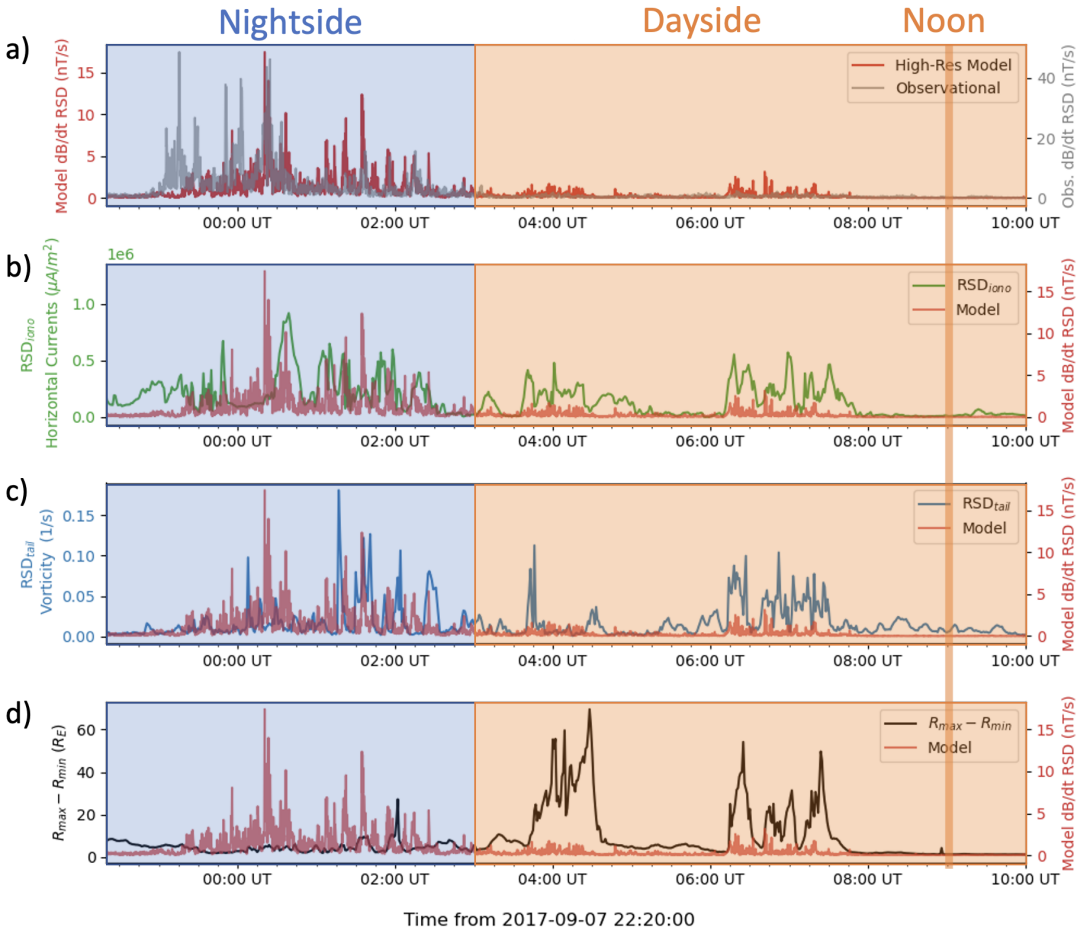

FIGURE 4.3: Marking whether the magnetometer stations are located on the dayside or the nightside throughout Part A of the storm from September 7, 22:00 UTC through September 8, 10:00 UTC.

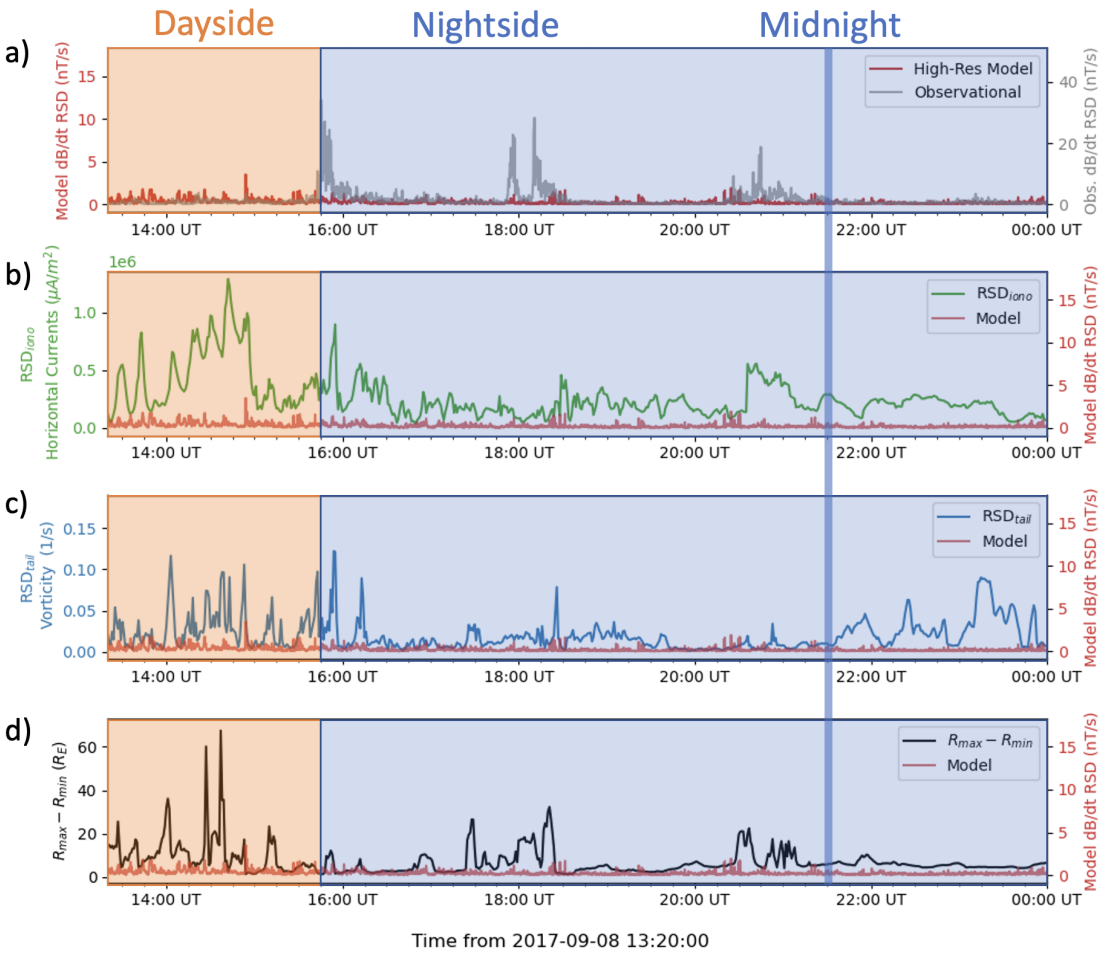

FIGURE 4.4: Marking whether the magnetometer stations are located on the dayside or the nightside throughout Part B of the storm from September 8, 13:00 UTC through September 9, 00:00 UTC.

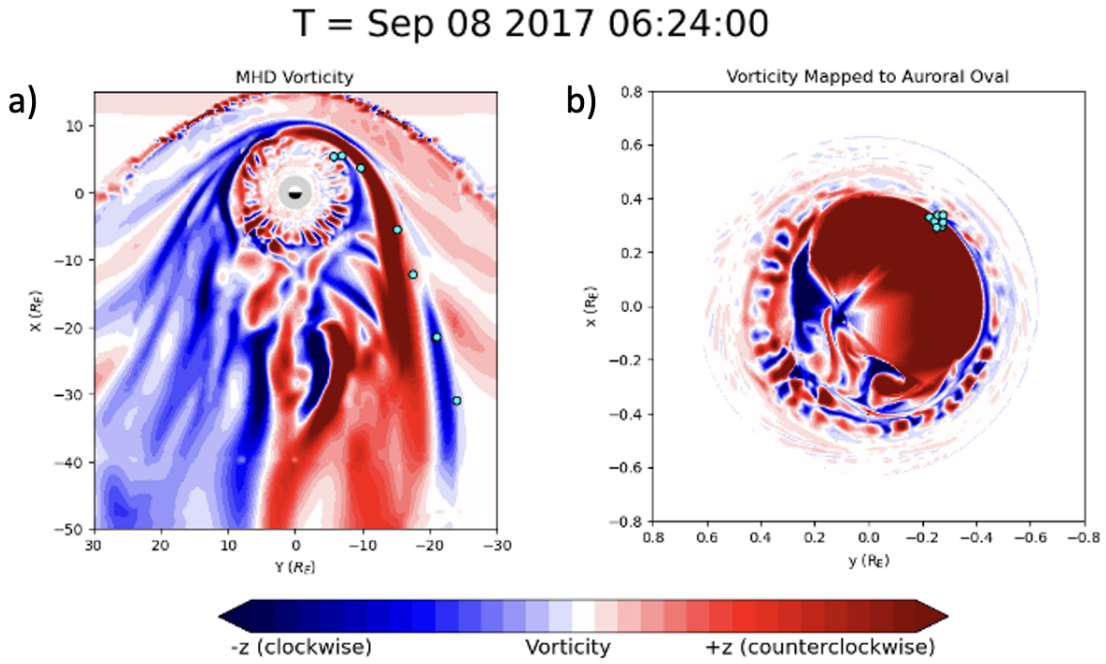

FIGURE 4.5: Vorticity contours with teal dots showing locations of magnetometer stations mapped from the ground along magnetic field lines. Panel a shows vorticity in the equatorial plane and panel b shows vorticity in the northern hemisphere. We see a spread of the stations down the tail as the station locations are caught in the shear flows along the magnetosheath.

the nightside and dayside. Throughout the storm, nightside station spread is less prevalent and lower magnitude than station spread during the times where stations are on the nightside. We are especially interested in the two peaks in station spread during the nightside of Figure 4.4, since they align with the second and third observational RSD peaks on the ground.

4.3 Station Spread

We have already correlated RSD and station spread in Figures 4.1, 4.2, 4.3, and 4.4, and now we visualize station spread in another way to examine the drivers of station spread during times when the stations are on the dayside, and times when the stations are on the nightside. Figure 4.5 shows station spread at September 8, 06:24 UT. This epoch occurs during a time when the stations are on the dayside in Figure 4.3. Figure 4.5a shows a slice through the X-Y equatorial plane at Z=0, looking down on Earth from above. Figure 4.5b shows the northern hemisphere. The colorbar indicates vorticity strength and direction, with red contours indicating vorticity coming out of the page in the +Z direction, and blue contours indicating vorticity entering the page in the -Z direction. The teal dots in Figure 4.5b indicate the station locations on the ground, and the teal dots in Figure 4.5a indicate where those station locations map along field lines. For this specific epoch of the model output, the station locations map to vastly disparate locations in the tail. Figure 4.5a shows that at this epoch, station locations in the equatorial plane are caught in a fast flow on the flank of the magnetosphere, and the magnetic field lines are swept downtail and separated from one another.

We can also capture information about the location of the last closed magnetic field lines in the model to determine if this boundary shows any relation to station spread. Figure 4.6 shows a similar plot to Figure 4.5 but plotting perpendicular velocity contours in the equatorial plane and the northern hemisphere on September 8, 06:18 UT. This epoch also occurs during a time when the stations are on the dayside in Figure 4.3. Figure 4.6a shows a slice through the X-Y

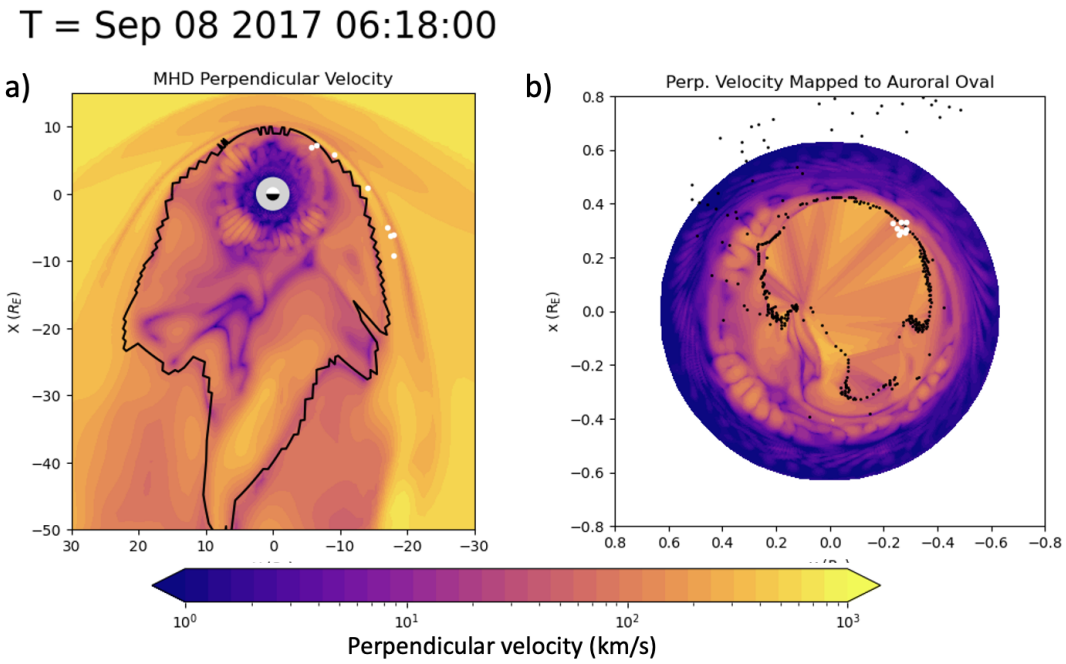

FIGURE 4.6: Perpendicular velocity contours with white dots showing locations of magnetometer stations mapped from the ground along magnetic field lines and black lines and dots showing the location of the last closed field line. Panel a shows perpendicular velocity in the equatorial plane and panel b shows perpendicular velocity in the northern hemisphere. Stations spread down the tail as the field lines approach the open-closed field line boundary.

equatorial plane at Z=0, looking down on Earth from above, showing magnetospheric activity in terms of perpendicular velocity and the boundary of the last closed magnetic field lines outlined in black. Figure 4.6b shows the northern hemisphere with the same perpendicular velocity contours and black dots indicating an approximate mapping of the last closed field line boundary locations from the equatorial plane. The colorbar indicates strength of the velocity. The white dots in Figure 4.6b show the station locations on the ground, and the white dots in Figure 4.6a indicate where those station locations map to along field lines. In this case, we again see the station locations in the equatorial plane being swept downtail as they interact with the open-closed field line boundary.

Additional note on Figure 4.6: the mapping of the last closed field line boundary to the northern hemisphere is imperfect - black dots that are meant to form a solid boundary are instead scattered around the northern hemisphere or even outside Earth. This is because while every other ray tracing technique we have utilized in this dissertation traces along field lines from the ionosphere out into the magnetosphere, this particular mapping moves from magnetosphere to ionosphere. Mapping from the ionosphere to the magnetosphere produces highly precise footpoints because the spatial resolution in the ionosphere is extremely high, and exact locations are easily resolved. However, the reverse is also true - mapping from the magnetosphere to the ionosphere is less precise because the spatial resolution of the magnetosphere is lower than the ionosphere.

Finally, we must examine an epoch during which station spread occurs while the stations are located on the nightside, as in the later part of Figure 4.4. We return to vorticity contours in Figure 4.7, which shows the same setup as Figure

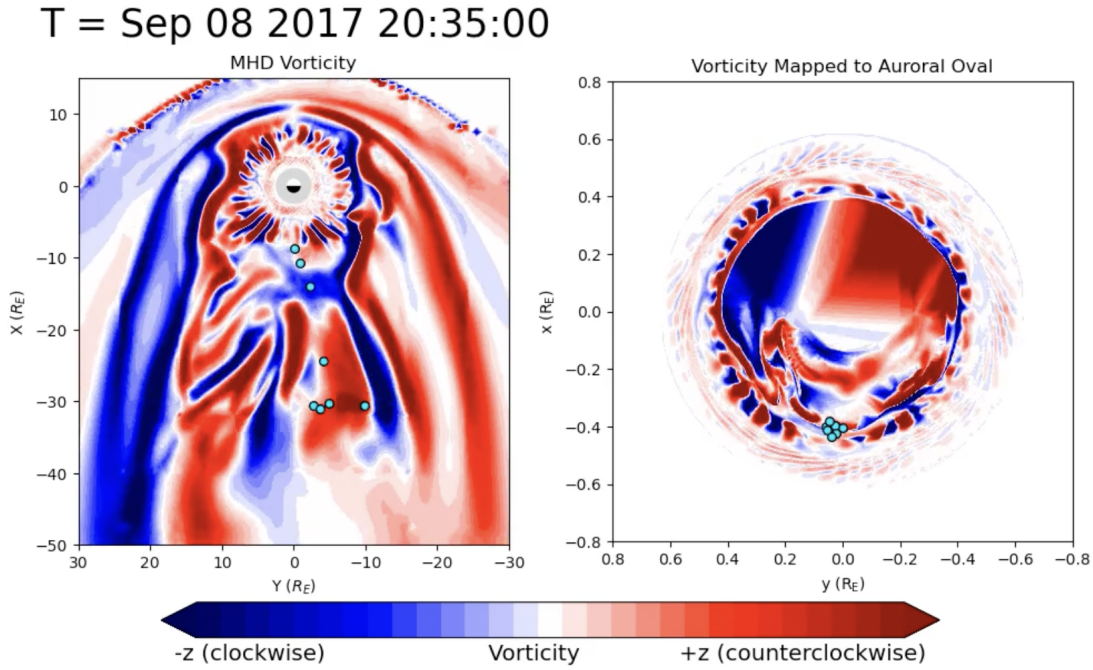

FIGURE 4.7: Vorticity contours with teal dots showing station locations in the equatorial plane and the northern hemisphere. We see that station spread occurs even when stations map to the middle of the tail, and not the open-closed field line boundary or a fast flow on the flank.

4.5 for the epoch Spetember 8, 20:35 UT. In Figure 4.7a we see the station footpoints caught in vorticity flows in the center of the magnetosphere, rather than on the flanks as seen in Figure 4.5. Because this period of time occurs during an observed LGMD, we can flag this region as containing possible drivers of LGMDs that are not captured on the ground.

4.4 Substorm Activity

Part B of the storm is associated with strong substorm activity (Clilverd et al., 2018; Dimmock et al., 2021), so we examine this period in the context of observable substorm signatures in the model. Studies of modeling substorms in global MHD show that we are able to capture substorm activity in a significant way starting with early efforts and continuing into the present. Lyon et al. (1998) shows global MHD reproducing polar cap flux values seen in observation during a substorm, and while there are differences between observation and simulation, it is clear a global picture of substorm activity can be obtained from MHD. Haiducek et al. (2020) has demonstrated that MHD can reproduce key ground-based signatures of substorms, such as AL-negative bays and mid-latitude signatures, although often with weaker amplitudes than in observation.

For this particular storm, the model does not show the manifestation of substorm activity in Part B as LGMDs on the ground. We examine other parts of the model to look for substorm signatures, particularly around September 8, 18:00 UT where the second peak in Figure 4.2a can be seen in observational dB/dt RSD but not in the model RSD on the ground. Figure 4.8 shows a slice through

the X-Z plane of the magnetosphere at the time of this disturbance on September 8, 18:42 UT. The contours illustrate thermal pressure, which is strongest in the ring current and plasmasheet but minimal throughout the lobes. The thick red lines illustrate the last-closed magnetic field lines; light black lines illustrate other magnetic field lines traced through the plane. These field lines show the clear development of a substorm expansion: a near-Earth reconnection line around $20R_E$ downtail and the spiraling field lines corresponding to a plasmoid. In subsequent minutes, the plasmoid is released and the newly reconnected closed field lines dipolarize. This is a textbook example of tail dynamics during a substorm and they occur in conjunction with the real-world substorm signatures. Despite good model-observation association, the model produces only weak ground signatures and a slight LGMD event. A discussion on the possible reasons that the model fails to translate the tail dynamics into a clear ground signature is presented in the next chapter.

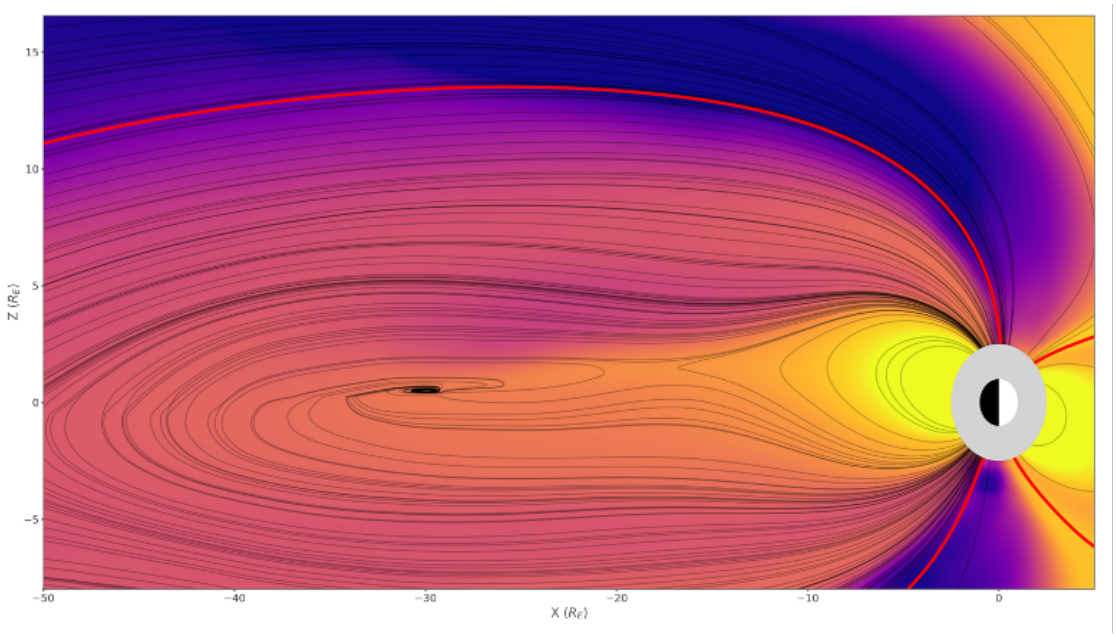

FIGURE 4.8: Magnetic field lines in an x-z slice of the magnetosphere during September 8, 18:42 UT. We see dipolarization indicating the presence of a substorm in the model, but the lack of modeled RSD activity during this time period indicates the energy transfer associated with the substorm does not translate down to the ground the way that observed reality indicates.

Chapter 5

Discussion & Conclusions

5.1 Summary

This dissertation has presented an examination of the understanding and predicting of LGMDs in global models for the purposes of building our knowledge of the Sun-Earth system, mitigating the effects of Space Weather, and growing our knowledge of the physics that drives LGMDs. Our analysis of the September 7, 2017 event leads us to several broad conclusions both about the drivers of LGMDs in the model during this event and about the ability of the SWMF to reproduce LGMDs. We can reproduce the period of increased LGMD activity seen in the first half of the storm, but we miss three large LGMDs in the second half of the storm. In the first half of the storm, the statistics indicate that although amplitudes of the LGMDs seen in the model are consistently smaller than the amplitudes of observed LGMDs, the overall occurrence of medium- and high-amplitudes LGMDs is similar between model and observation. The difference in amplitudes will be discussed in th efollowing section. Overall analysis also includes the confirmation that the high-resolution configuration

is required in order for the SWMF to reproduce LGMDs in a meaningful way. Our broad conclusions about the drivers of LGMDs come from examining the J_ϕ RSD$_{iono}$ and ω RSD$_{tail}$. We see that the main drivers of LGMDs during the first half of the storm are small spatial scale magnetospheric and ionospheric activity. An important set of conclusions gleaned from the model results and comparison are the implications of station spread. Several times during this event we see a clear correlation between station spread, magnetospheric vorticity, and horizontal ionospheric currents. These time periods do translate to small-magnitude RSD spikes on the ground. This shows that large-scale storm dynamics in the magnetosphere can map down to small-scale features in the ionosphere and down to the ground. Although we do not see clear drivers for the LGMDs in the second half of the storm, we see station spread coinciding with multiple observed periods of LGMDs that mark station spread as a potential driver of LGMDs. A discussion on the missing LGMDs and the potential of station spread will be considered in the discussion section.

5.2 Discussion

A likely reason behind the lower LGMD magnitude in the model is the empirical conductance model (Mukhopadhyay et al., 2022; Mukhopadhyay et al., 2020) employed in these simulations. Ionospheric conductance remains an outstanding challenge for global MHD simulations, especially concerning predictions of ground magnetic perturbations (Welling et al., 2017; Welling, 2019). The

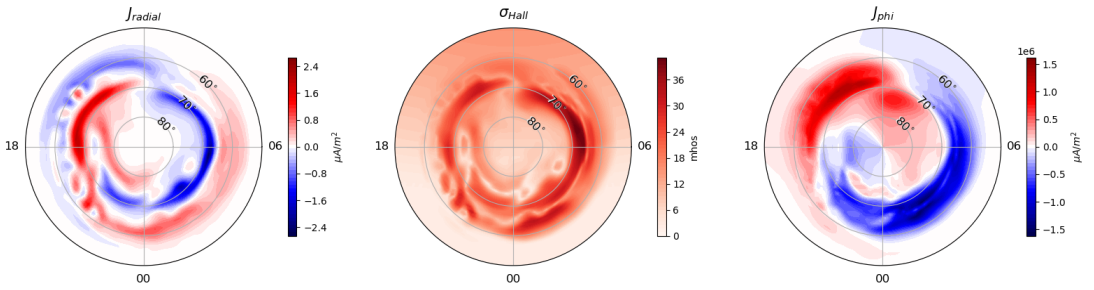

FIGURE 5.1: FAC, Hall Conductance, Horiz currents

empirical model employed here is an empirical relationship between conductance and local FAC strength. The auroral oval location is fit to upward FAC and an additional conductance term is applied broadly over the oval. The result is a conductance pattern that is smooth and spatially broad, allowing horizontal currents to close over a wide area. This means that FACs driven by small scale features in the magnetosphere (for example, the localization of vorticity or flow shears illustrated in Figures 3.6 and 4.1) can disperse once they arrive at the ionosphere as their closure path is broad. Real world auroral features and, therefore, conductance channels, can be narrow and complex. FACs closing through these conductance bands form narrow electrojets, concentrating current to smaller areas.

So long as the basic empirical conductance model is used, many mechanisms for generating LGMDs in the SWMF will be circumvented. With the current conductance model, these currents become "smeared" across the ionosphere, giving the false impression that flow channels and other ionosphere phenomena are more spread out than in observed reality. This causes RSD in the model to be weaker, which is reflected in the amplitude difference between model RSD and

observed RSD. An example of this is shown in Figure 5.1. 5.1a shows the field-aligned currents in the northern hemisphere at the same epoch as Figure 4.8 - September 8, 18:42 UT. We see that the SWMF resolves these currents well, showing good localized structure during enhanced ionospheric activity. In Figure 5.1b, we see Hall conductance calculated using the empirical conductance model. In Figure 5.1c, we see the horizontal currents in the ionosphere. While the SWMF captures the approximate shape of the horizontal currents, we can clearly see the smearing that occurs as a result of the conductance. While these diffused currents can be useful in observing global phenomena, localized features are much more difficult to resolve. Transitioning from the legacy empirical conductance model to an advanced physics-based approach that retains small scale structure will be a critical next step in LGMD research.

To address the problem of missing LGMDs in the model, we can also discuss the implications of a potential link between substorms and nightside station spread. We see slight correlation of station spread with observed RSD spikes on the ground during the time when the stations are on the nightside. Combined with the knowledge that substorm activity is occurring in the model during both periods of nightside station spread, we can see the potential for substorm dipolarization and plasma transport to act as drivers of this station spread. In this case, two issues would prevent the dynamics of a substorm from translating into LGMDs on the ground. First, we know that historically the SWMF can capture ionospheric convection and accurately reproduce magnetic field geometry (Welling, 2019). However, we also know that the tail reconnection rate in the SWMF is slower than in reality which in turn affects the rate of plasma transport

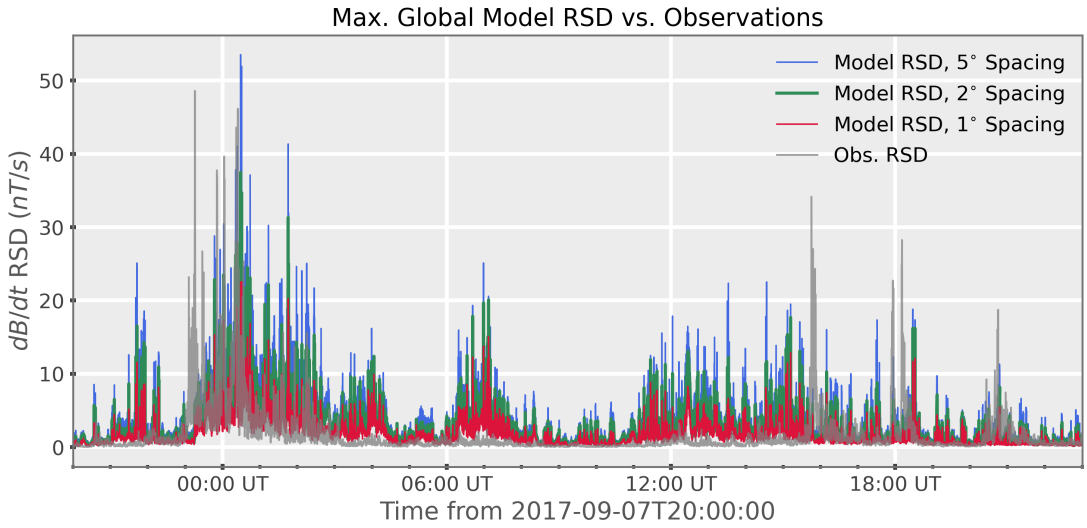

FIGURE 5.2: dB/dt RSD as observed (light gray line) and maximum global RSD from the simulation result using a $1^\circ \times 1^\circ$ stencil (red line), a $2^\circ \times 2^\circ$ stencil (green line), and a $5^\circ \times 5^\circ$ stencil (blue line).

toward Earth during substorms. This could result in poor accuracy and strength of the dynamics driving station spread. Second, the station spread captured in the model does not always translate to RSD spikes on the ground. Further study would explore the possibility of a more complex coupling between the spreading of magnetic field lines and the potential for such magnetospheric effects to appear in ground magnetic perturbations.

Another possible explanation for the RSD spikes absent from the model is the possibility that the model does capture them, but not in the precise locations we are examining. Reproducing LGMDs requires that the model precisely captures the precise location of the source of LGMDs, both in the magnetosphere and the ionosphere. Small discrepancies in source location can greatly degrade data-model comparisons, even though the physics of the model may have performed

admirably overall.

To explore the potential of this issue, a global maximum dB/dt RSD was calculated from the model. Virtual magnetometers were placed at a $1^\circ \times 1^\circ$ latitude-longitude spacing across the entire northern hemisphere. A 4-point, $1^\circ \times 1^\circ$ stencil was used to calculate RSD in one location. This stencil was then shifted by 1° in longitude and RSD was calculated again. This process was repeated over the full range of longitudes, then the stencil was shifted 1° in latitude and the longitude range scanned again. Once the stencil has been shifted across the entire northern hemisphere, the maximum RSD was saved and the process repeated for all points.

Figure 5.2 shows the result of this process. The red line is the global RSD from the entire northern hemisphere; the gray line is the observations-based RSD for reference. Compared to the model RSD drawn only from the stations listed in Table 2.1, there is substantially more LGMD activity. RSD spikes are more frequent in time and have a much higher typical amplitude, now rivaling the amplitudes of the observations-based values. There is extensive LGMD activity outside of the periods where such activity was observed, but this is not surprising as the model RSD values in this figure represent activity anywhere across the globe compared to the limited range represented by the magnetomters used in the observational set. Notably, there is much more LGMD activity during the three main substorm related spikes, with a significant RSD spike occurring near the observed spikes near 18:00UT. This figure demonstrates that the SWMF is indeed capable of producing significant localization of GMD activity, including activity related to substorms. However, there is much work remaining to

improve the location of such spikes to better represent real-world activity.

While the model RSD magnitudes in Figure 5.2 better correspond to those from the observations, the largest values are still not achieved. This leaves open the question that model may not be capturing LGMD development on the same scale as the real world. To investigate this further, the process used to create the red line in Figure 5.2 was repeated, but with progressively larger stencil sizes that include more points for each RSD calculation. For example, a $3^\circ \times 3^\circ$ stencil would include $3 \times 3 = 9$ virtual magnetometer points simultaneously. Each stencil was still only shifted 1° per iteration. Stencil sizes from 1° to 5° were used to see at what point RSD magnitude stopped growing, indicating that the stencil is now larger than typical GMD spatial scale sizes. The green and blue lines in Figure 5.2 show the global RSD results for 2° and 5° stencil sizes, respectively. Extending the stencil size from 1° to 2° (red to green line) dramatically increases the resulting RSD magnitude, indicating that model activity is better characterized on 2° latitude/longitude scales. These scales show much better agreement with the observed magnitudes overall, especially early in the event simulation. Beyond this size, amplitudes change far more modestly. The results for 5° stencil sizes (blue line) are very similar to the 2° spacing, indicating that most activity is captured at the finer stencil size. Overall, this comparison demonstrates that the SWMF is capturing smaller scale GMD dynamics, but further work may be required to drive this down to observed scales. This may include further refining the magnetosphere and ionosphere numerical grid or employing better auroral physics as described above.

5.3 Future Work

Next steps in this study will involve replacing the empirical conductance calculation in the SWMF with a physics-based conductance calculation, the MAGnetosphere Ionosphere Thermosphere (MAGNIT) model (Mukhopadhyay et al., 2022). Because the prediction of LGMDs relies on the location accuracy of ionospheric currents, implementing MAGNIT will improve both the accuracy and amplitude of LGMD predictions. Conductance and current smearing shown in Figure 5.1 will improve, and the ionosphere will show small-scale structure that will directly translate to LGMDs on the ground. Improvements from MAGNIT may also shed light on the issue of substorm energy transfer to the ground.

An additional next step for this work is to couple a ground conductivity model to the high-resolution SWMF output and use the same metrics to quantify improvements. Dimmock et al. (2021) factors telluric currents into the SWMF output in Fennoscandia and shows correlation between observed and modeled ground magnetic perturbations and GICs. Marshalko et al. (2021) models electric field and ground magnetic perturbations using a 3-D conductivity model in the same geographical region. Further work will seek to include ground conductivity and telluric currents to improve prediction power and explore more drivers of LGMDs.

This dissertation has thoroughly explored LGMDs in numerical models during a period of storm time using both existing and new metrics to compare different regions of the simulation to observed LGMDs. We note a statistically significant ability to reproduce observed LGMD, identify clear drivers of LGMDs

in the model, clearly note the limitations of the model regarding LGMDs, hypothesize various causes for these model deficiencies, and propose model improvements that will directly address these deficiencies. This work is a valuable step towards understanding LGMDs and improving Space Weather prediction ability.

Bibliography

Apatenkov, S. V., Pilipenko, V. A., Gordeev, E. I., Viljanen, A., Juusola, L., Belakhovsky, V. B., Sakharov, Y. A., & Selivanov, V. N. (2020). Auroral Omega Bands are a Significant Cause of Large Geomagnetically Induced Currents. *Geophysical Research Letters*. https://doi.org/10.1029/2019GL086677

Baker, D. N., Pulkkinen, T., Angelopoulos, V., Baumjohann, W., & McPherron, R. (1996). Neutral line model of substorms: Past results and present view. *Journal of Geophysical Research: Space Physics*, *101*(A6), 12975–13010.

Baumjohann, W., & Treumann, R. A. (2012). *Basic space plasma physics (revised edition)*. https://doi.org/10.1142/P850

Birn, J., Raeder, J., Wang, Y. L., Wolf, R. A., & Hesse, M. (2004). On the propagation of bubbles in the geomagnetic tail. *22*, 1773–1786.

Blake, S. P., Pulkkinen, A., Schuck, P. W., Glocer, A., & Tóth, G. (2021). Estimating Maximum Extent of Auroral Equatorward Boundary Using Historical and Simulated Surface Magnetic Field Data. *Journal of Geophysical Research: Space Physics*, *126*(2), e2020JA028284. https://doi.org/10.1029/2020JA028284

Borovsky, J. E., Delzanno, G. L., Valdivia, J. A., Moya, P. S., Stepanova, M., Birn, J., Blum, L. W., Lotko, W., & Hesse, M. (2020). Outstanding questions

in magnetospheric plasma physics: The pollenzo view. *Journal of Atmospheric and Solar-Terrestrial Physics*, *208*, 105377.

Boteler, D. H. (2019). A 21st century view of the march 1989 magnetic storm. *Space Weather*, *17*(10), 1427–1441. https://doi.org/https://doi.org/10.1029/2019SW002278

Boteler, D. H., Pirjola, R. J., & Nevanlinna, H. (1998). The effects of geomagnetic disturbances on electrical systems at the Earth's surface. *Advances in Space Research*, *22*(1), 17–27. https://doi.org/10.1016/S0273-1177(97)01096-X

Clilverd, M. A., Rodger, C. J., Brundell, J. B., Dalzell, M., Martin, I., Manus, D. H. M., Thomson, N. R., Petersen, T., & Obana, Y. (2018). Long-lasting geomagnetically induced currents and harmonic distortion observed in new zealand during the 7–8 september 2017 disturbed period. *Space Weather*, *16*. https://doi.org/10.1029/2018SW001822

Cowley, S. W. (2000). *Magnetosphere-ionosphere interactions: A tutorial review* (Vol. 118). https://doi.org/10.1029/GM118p0091

DeZeeuw, D. L., Sazykin, S., Wolf, R. A., Gombosi, T. I., Ridley, A. J., & Tóth, G. (2004). Coupling of a global mhd code and an inner magnetospheric model: Initial results. *Journal of Geophysical Research: Space Physics*, *109*. https://doi.org/10.1029/2003JA010366

Dimmock, A. P., Rosenqvist, L., Hall, J. O., Viljanen, A., Yordanova, E., Honkonen, I., André, M., & Sjöberg, E. C. (2019). The GIC and Geomagnetic Response Over Fennoscandia to the 7–8 September 2017 Geomagnetic Storm. *Space Weather*. https://doi.org/10.1029/2018SW002132

Dimmock, A. P., Rosenqvist, L., Welling, D. T., Viljanen, A., Honkonen, I., Boynton, R. J., & Yordanova, E. (2020). On the Regional Variability of dB/dt and Its Significance to GIC. *Space Weather*, *18*(8), 1–20. https://doi.org/10.1029/2020SW002497

Dimmock, A. P., Welling, D. T., Rosenqvist, L., Forsyth, C., Freeman, M. P., Rae, I. J., Viljanen, A., Vandegriff, E., Boynton, R. J., Balikhin, M. A., & Yordanova, E. (2021). Modeling the Geomagnetic Response to the September 2017 Space Weather Event Over Fennoscandia Using the Space Weather Modeling Framework: Studying the Impacts of Spatial Resolution. *Space Weather*, *19*(5), 1–30. https://doi.org/10.1029/2020SW002683

Dungey, J. W. (1961). Interplanetary magnetic field and the auroral zones. *Phys. Rev. Lett.*, *6*, 47–48. https://doi.org/10.1103/PhysRevLett.6.47

Dungey, J. W. (1963). Interactions of solar plasma with the geomagnetic field. *Planetary and Space Science*, *10*(100), 233–237. https://doi.org/10.1016/0032-0633(63)90020-5

Erickson, G., & Wolf, R. (1980). Is steady convection possible in the earth's magnetotail? *Geophysical Research Letters*, *7*(11), 897–900.

Eshetu, W. W., Lyon, J. G., Hudson, M. K., & Wiltberger, M. J. (2019). Simulations of Electron Energization and Injection by BBFs Using High-Resolution LFM MHD Fields. *Journal of Geophysical Research: Space Physics*, *124*(2), 1222–1238. https://doi.org/10.1029/2018JA025789

Garcia-Sage, K., Moore, T. E., Pembroke, A., Merkin, V. G., & Hughes, W. J. (2015). Modeling the effects of ionospheric oxygen outflow on bursty

magnetotail flows. *Journal of Geophysical Research: Space Physics*, *120*(10), 8723–8737. https://doi.org/10.1002/2015JA021228

Genestreti, K., Kistler, L., & Mouikis, C. (2012). *The role and dynamics of oxygen of ionospheric origin in magnetopause reconnection* (Doctoral dissertation). https://doi.org/10.13140/2.1.4788.2882

Gombosi, T. I., & Holman, G. D. (1999). Physics of the space environment. *Physics Today*, *52*, 62–63. https://doi.org/10.1063/1.882826

Gonzalez, W., Joselyn, J.-A., Kamide, Y., Kroehl, H. W., Rostoker, G., Tsurutani, B., & Vasyliunas, V. (1994). What is a geomagnetic storm? *Journal of Geophysical Research: Space Physics*, *99*(A4), 5771–5792.

Haiducek, J. D., Welling, D. T., Morley, S. K., Ganushkina, N. Y., & Chu, X. (2020). Using Multiple Signatures to Improve Accuracy of Substorm Identification. *Journal of Geophysical Research: Space Physics*. https://doi.org/10.1029/2019JA027559

Kappenman, J. G. (1996). Geomagnetic storms and their impact on power systems. *IEEE Power Engineering Review*, *16*(5), 5. https://doi.org/10.1109/MPER.1996.491910

Kivelson, M. G., Russell, C. T., & Brown, M. E. (1996). Introduction to space physics. *Physics Today*, *49*. https://doi.org/10.1063/1.2807586

Le, G., Slavin, J. A., & Strangeway, R. J. (2010). Space technology 5 observations of the imbalance of regions 1 and 2 field-aligned currents and its implication to the cross-polar cap pedersen currents. *Journal of Geophysical Research: Space Physics*, *115*. https://doi.org/10.1029/2009ja014979

Lyon, J. G., Lopez, R. E., Goodrich, C. C., Wiltberger, M., & Papadopoulos, K. (1998). Simulation of the march 9, 1995, substorm: Auroral brightening and the onset of lobe reconnection. *Geophysical Research Letters*, *25*(15), 3039–3042. https://doi.org/https://doi.org/10.1029/98GL00662

Lyons, L. R., Nishimura, Y., Zhang, S., Coster, A., Liu, J., Bristow, W. A., Reimer, A. S., Varney, R. H., & Hampton, D. L. (2021). Direct Connection Between Auroral Oval Streamers/Flow Channels and Equatorward Traveling Ionospheric Disturbances. *Frontiers in Astronomy and Space Sciences*, *8*(October), 1–15. https://doi.org/10.3389/fspas.2021.738507

Lysak, R. L. (1990). Electrodynamic coupling of the magnetosphere and ionosphere. *Space Science Reviews*, *52*. https://doi.org/10.1007/BF00704239

Marshalko, E., Kruglyakov, M., Kuvshinov, A., Juusola, L., Kwagala, N. K., Sokolova, E., & Pilipenko, V. (2021). Comparing three approaches to the inducing source setting for the ground electromagnetic field modeling due to space weather events. *Space Weather*, *19*. https://doi.org/10.1029/2020SW002657

Molinski, T. S. (2002). Why utilities respect geomagnetically induced currents. *Journal of Atmospheric and Solar-Terrestrial Physics*, *64*(16), 1765–1778. https://doi.org/10.1016/S1364-6826(02)00126-8

Morley, S. K., Brito, T. V., & Welling, D. T. (2018). Measures of model performance based on the log accuracy ratio. *Space Weather*, *16*, 69–88. https://doi.org/10.1002/2017SW001669

Mukhopadhyay, A., Welling, D., Liemohn, M., Ridley, A., Burleigh, M., Wu, C., Zou, S., Connor, H., Vandegriff, E., Dredger, P., & Tóth, G. (2022). Global

driving of auroral precipitation: 1. balance of sources. *Journal of Geophysical Research: Space Physics*, *127*. https://doi.org/10.1029/2022JA030323

Mukhopadhyay, A., Welling, D. T., Liemohn, M. W., Ridley, A. J., Chakraborty, S., & Anderson, B. J. (2020). Conductance Model for Extreme Events: Impact of Auroral Conductance on Space Weather Forecasts. *Space Weather*, *18*(11). https://doi.org/10.1029/2020SW002551

Ngwira, C. M., & Pulkkinen, A. A. (2019). An introduction to geomagnetically induced currents. In *Geomagnetically induced currents from the sun to the power grid*. https://doi.org/10.1002/9781119434412.ch1

Ngwira, C. M., Pulkkinen, A. A., Bernabeu, E., Eichner, J., Viljanen, A., & Crowley, G. (2015). Characteristics of extreme geoelectric fields and their possible causes: Localized peak enhancements. *Geophysical Research Letters*, *42*(17), 6916–6921. https://doi.org/10.1002/2015GL065061

Ngwira, C. M., Sibeck, D., Silveira, M. V., Georgiou, M., Weygand, J. M., Nishimura, Y., & Hampton, D. (2018). A Study of Intense Local dB/dt Variations During Two Geomagnetic Storms. *Space Weather*, *16*(6), 676–693. https://doi.org/10.1029/2018SW001911

Nishimura, Y., Lyons, L. R., Angelopoulos, V., Kikuchi, T., Zou, S., & Mende, S. B. (2011). Relations between multiple auroral streamers, pre-onset thin arc formation, and substorm auroral onset. *Journal of Geophysical Research: Space Physics*, *116*(A9), 9214. https://doi.org/10.1029/2011JA016768

Nishimura, Y., Lyons, L. R., Shiokawa, K., Angelopoulos, V., Donovan, E. F., & Mende, S. B. (2013). Substorm onset and expansion phase intensification

precursors seen in polar cap patches and arcs. *Journal of Geophysical Research: Space Physics*, *118*(5), 2034–2042. https://doi.org/10.1002/JGRA.50279

Nishimura, Y., Lessard, M. R., Katoh, Y., Miyoshi, Y., Grono, E., Partamies, N., Sivadas, N., Hosokawa, K., Fukizawa, M., Samara, M., Michell, R. G., Kataoka, R., Sakanoi, T., Whiter, D. K., ichiro Oyama, S., Ogawa, Y., & Kurita, S. (2020). Diffuse and Pulsating Aurora. *Space Science Reviews 2020 216:1*, *216*(1), 1–38. https://doi.org/10.1007/S11214-019-0629-3

Ohtani, S., & Yoshikawa, A. (2016). The initiation of the poleward boundary intensification of auroral emission by fast polar cap flows: A new interpretation based on ionospheric polarization. *Journal of Geophysical Research: Space Physics*, *121*(11), 10, 910–10, 928. https://doi.org/10.1002/2016JA023143

Pulkkinen, A., Rastätter, L., Kuznetsova, M., Singer, H., Balch, C., Weimer, D., Toth, G., Ridley, A., Gombosi, T., Wiltberger, M., Raeder, J., & Weigel, R. (2013). Community-wide validation of geospace model ground magnetic field perturbation predictions to support model transition to operations. *Space Weather*. https://doi.org/10.1002/swe.20056

Pulkkinen, A. (2015). Geomagnetically Induced Currents Modeling and Forecasting. https://doi.org/10.1002/2015SW001316

Ridley, A. J., Gombosi, T. I., & DeZeeuw, D. L. (2004). Ionospheric control of the magnetosphere: Conductance. *Annales Geophysicae*, *22*. https://doi.org/10.5194/angeo-22-567-2004

Russell, C. T., McPherron, R. L., & Burton, R. K. (1974). On the cause of geomagnetic storms. *Journal of Geophysical Research*, *79*. https://doi.org/10.1029/ja079i007p01105

Sergeev, V. A., Liou, K., Newell, P. T., Ohtani, S.-I., Hairston, M. R., & Rich, F. (2004). Auroral streamers: characteristics of associated precipitation, convection and field-aligned currents. *22*, 537–548.

Tóth, G., Sokolov, I. V., Gombosi, T. I., Chesney, D. R., Clauer, C. R., De Zeeuw, D. L., Hansen, K. C., Kane, K. J., Manchester, W. B., Oehmke, R. C., Powell, K. G., Ridley, A. J., Roussev, I. I., Stout, Q. F., Volberg, O., Wolf, R. A., Sazykin, S., Chan, A., Yu, B., & Kóta, J. (2005). Space Weather Modeling Framework: A new tool for the space science community. *Journal of Geophysical Research: Space Physics*, *110*(A12), 12226. https://doi.org/10.1029/2005JA011126

Viljanen, A., Tanskanen, E. I., & Pulkkinen, A. (2006). Relation between substorm characteristics and rapid temporal variations of the ground magnetic field. *Annales Geophysicae*. https://doi.org/10.5194/angeo-24-725-2006

Vokhmyanin, M., Apatenkov, S., Gordeev, E., Andreeva, V., Partamies, N., Kauristie, K., & Juusola, L. (2021). Statistics on Omega Band Properties and Related Geomagnetic Variations. *Journal of Geophysical Research: Space Physics*, *126*(7). https://doi.org/10.1029/2021JA029468

Wanliss, J. A., & Showalter, K. M. (2006). High-resolution global storm index: Dst versus sym-h. *Journal of Geophysical Research: Space Physics*, *111*. https://doi.org/10.1029/2005JA011034

Wei, D., Dunlop, M. W., Yang, J., Dong, X., Yu, Y., & Wang, T. (2021). Intense dB/dt Variations Driven by Near-Earth Bursty Bulk Flows (BBFs): A Case Study. *Geophysical Research Letters*, *48*(4). https://doi.org/10.1029/2020GL091781

Welling, D. T., Anderson, B. J., Crowley, G., Pulkkinen, A. A., & Rastätter, L. (2017). Exploring predictive performance: A reanalysis of the geospace model transition challenge. *Space Weather*, *15*. https://doi.org/10.1002/2016SW001505

Welling, D. T., & Liemohn, M. W. (2014). Outflow in global magnetohydrodynamics as a function of a passive inner boundary source. *Journal of Geophysical Research: Space Physics*, *119*(4), 2691–2705. https://doi.org/https://doi.org/10.1002/2013JA019374

Welling, D. T., Ngwira, C. M., Opgenoorth, H., Haiducek, J. D., Savani, N. P., Morley, S. K., Cid, C., Weigel, R. S., Weygand, J. M., Woodroffe, J. R., Singer, H. J., Rosenqvist, L., & Liemohn, M. W. (2018). Recommendations for Next-Generation Ground Magnetic Perturbation Validation. *Space Weather*. https://doi.org/10.1029/2018SW002064

Welling, D. (2019). Magnetohydrodynamic Models of B and Their Use in GIC Estimates. https://doi.org/10.1002/9781119434412.ch3

Wiltberger, M., Merkin, V., Lyon, J. G., & Ohtani, S. (2015). High-resolution global magnetohydrodynamic simulation of bursty bulk flows. *Journal of Geophysical Research: Space Physics*, *120*(6), 4555–4566. https://doi.org/10.1002/2015JA021080

Yang, J., Toffoletto, F. R., Wolf, R. A., Sazykin, S., Ontiveros, P. A., & Weygand, J. M. (2012). Large-scale current systems and ground magnetic disturbance during deep substorm injections. *Journal of Geophysical Research: Space Physics*, *117*(4). https://doi.org/10.1029/2011JA017415

Zou, Y., Dowell, C., Ferdousi, B., Lyons, L., Liu, J., Angelopoulos, V., & Mende, S. (2021). Auroral drivers of intense dbdt during geomagnetic storms. *AGUFM*, *2021*, SM34A–06.